



HAL
open science

Issues in growing Heusler compounds in thin films for spintronic applications

C. Guillemard, S. Petit-Watelot, T. Devolder, L. Pasquier, P. Boulet, S. Migot, J. Ghanbaja, F. Bertran, S. Andrieu

► **To cite this version:**

C. Guillemard, S. Petit-Watelot, T. Devolder, L. Pasquier, P. Boulet, et al.. Issues in growing Heusler compounds in thin films for spintronic applications. *Journal of Applied Physics*, 2020, 128 (24), pp.241102. 10.1063/5.0014241 . hal-04064714

HAL Id: hal-04064714

<https://hal.science/hal-04064714>

Submitted on 11 Apr 2023


HAL is a multi-disciplinary open access archive for the deposit and dissemination of scientific research documents, whether they are published or not. The documents may come from teaching and research institutions in France or abroad, or from public or private research centers.

L'archive ouverte pluridisciplinaire **HAL**, est destinée au dépôt et à la diffusion de documents scientifiques de niveau recherche, publiés ou non, émanant des établissements d'enseignement et de recherche français ou étrangers, des laboratoires publics ou privés.

Issues in growing Heusler compounds in thin films for spintronic applications

Cite as: J. Appl. Phys. **128**, 241102 (2020); <https://doi.org/10.1063/5.0014241>

Submitted: 18 May 2020 . Accepted: 05 December 2020 . Published Online: 30 December 2020

 C. Guillemard,  S. Petit-Watelot,  T. Devolder, L. Pasquier,  P. Boulet, S. Migot, J. Ghanbaja,  F. Bertran, and  S. Andrieu



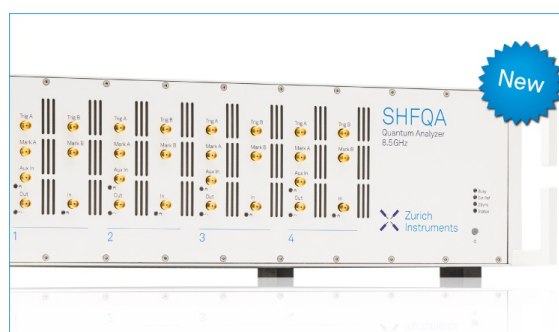
View Online



Export Citation



CrossMark



Your Qubits. Measured.

Meet the next generation of quantum analyzers

- Readout for up to 64 qubits
- Operation at up to 8.5 GHz, mixer-calibration-free
- Signal optimization with minimal latency

Find out more



Issues in growing Heusler compounds in thin films for spintronic applications

Cite as: J. Appl. Phys. 128, 241102 (2020); doi: 10.1063/5.0014241

Submitted: 18 May 2020 · Accepted: 5 December 2020 ·

Published Online: 30 December 2020



C. Guillemard,^{1,2,a)} S. Petit-Watelot,¹ T. Devolder,³ L. Pasquier,¹ P. Boulet,¹ S. Migot,¹ J. Chanbaja,¹ F. Bertran,² and S. Andrieu^{1,a)}

AFFILIATIONS

¹Institut Jean Lamour, Université de Lorraine—CNRS, UMR7198, 54011 Nancy, France

²Synchrotron SOLEIL—CNRS, L'Orme des Merisiers, 91192 Gif-sur-Yvette, France

³Centre de Nanosciences et de Nanotechnologies, CNRS, Université Paris-Saclay, 91120 Palaiseau, France

^{a)}Authors to whom correspondence should be addressed: cguillemard@gmail.com and stephane.andrieu@univ-lorraine.fr

ABSTRACT

Heusler magnetic alloys offer a wide variety of electronic properties very promising for spintronics and magnonics. Some alloys exhibit a spin gap in their band structure at the Fermi energy, the so-called half-metal magnetic (HMM) behavior. This particular property leads to two very interesting properties for spintronics, i.e., fully polarized current together with ultra-low magnetic damping, two key points for spin-transfer-torque based devices. This Tutorial gives experimental details to grow and characterize Heusler Co_2MnZ compounds in thin films ($Z = \text{Al, Si, Ga, Ge, Sn, Sb}$) by using molecular beam epitaxy in order to get the proper predicted electronic properties. A first part of this Tutorial is dedicated to control the stoichiometry as best as possible with some methods to test it. The chemical ordering within the lattice was examined by using electron diffraction during growth, regular x-ray diffraction, and scanning transmission electron microscopy. In particular, standard x-ray diffraction is carefully analyzed depending on the chemical ordering in the cubic cell and shown to be inefficient to distinguish several possible phases, on the contrary to electron microscopy. The electronic properties, i.e., magnetic moment, spin polarization, and magnetic damping were reviewed and discussed according to the stoichiometry of the films and also theoretical predictions. Polycrystalline films were also analyzed, and we show that the peculiar HMM properties are not destroyed, a good news for applications. A clear correlation between the spin polarization and the magnetic damping is experimentally demonstrated. At least, our study highlights the major role of stoichiometry on the expected properties.

Published under license by AIP Publishing. <https://doi.org/10.1063/5.0014241>

I. INTRODUCTION

Discovering new materials with outstanding properties represents a common challenge in all fields of condensed matter physics. Among those fields, some crucial goals of spintronics that aims to manipulate spin and charge currents together with the magnetization of nanometric-scaled structures are to increase the storage density in magnetic based memories as well as lowering their energy consumption. To do that, materials with very specific properties such as a full spin polarization (noted SP in the following) at the Fermi energy (E_F) along with a small Gilbert magnetic damping are required to reduce the critical switching current using spin transfer torques.¹ In 1983, de Groot *et al.*² discovered by using *ab initio* calculations a new type of ferromagnet, called half metal magnet (HMM), in which the majority spin electrons are metallic, whereas minority spin ones are insulating. In other words, the

density of electronic states contains a gap near the Fermi energy E_F in the minority spin channel resulting in a full SP at E_F . This new type of ferromagnet satisfies in theory the requirements for a new era in spintronics and magnonics. Since the predictions of de Groot *et al.*, huge theoretical efforts have been made to identify materials with the HMM property that are convenient to elaborate. Such HMM properties were first observed in magnetic oxides (Fe_3O_4 , CrO_2 , LaSrMnO_3) but were at least difficult to implement in spintronics devices due to small magnetizations at remanence or too low Curie temperatures (see Ref. 3 and references therein). As the de Groot theoretical work was done on the half-Heusler NiMnSb compound,² a lot of other Heusler compounds were thus explored using *ab initio* calculations^{4–9} and a spin gap was calculated in some of them (Co_2MnSi ,⁴ Co_2CrSi ,⁹ Fe_2MnGa ,¹⁰ Mn_2ScGe ,¹¹ etc.). But beyond the spin gap, these compounds are

also very interesting because some have high Curie temperatures well above room temperature,^{12,13} which is important for device stability. The initial interest in growing Heusler thin films was, therefore, to demonstrate and obtain a spin gap and a complete SP. Although huge TMR values were expected in Heusler-MgO based magnetic tunnel junctions (MTJs),¹⁴ the first reported results obtained on spin polarization^{15–17} and on devices^{18–20} then remained disappointing. At this time, with such poor properties, Heusler-based thin films could in no way compete with the basic CoFeB/MgO system used in devices. Fortunately, the interest for these compounds was completely renewed, thanks to the remarkable transport results obtained after 2009^{21–23} using Co₂MnSi in MgO-based magnetic tunnel junctions (MTJs). As a consequence, further experiments using spin-resolved photoemission spectroscopy (SR-PES) were performed on this particular material and the spin gap was observed,^{3,24} which definitely confirms the HMM behavior of Co₂MnSi. In parallel, another remarkable property of these compounds was highlighted theoretically. Very low magnetic damping values in the range of 10⁻⁵–10⁻⁴ were calculated for some HMM Heuslers.^{25–27} Such a property is crucial to considerably reduce the magnetization reversal currents by spin transfer torque or to extend spin-wave propagation length. From this point of view, HMM Heusler compounds have a big advantage over the CoFeB/MgO system principally used in spintronic devices, for which magnetic damping values not better than 5 × 10⁻³ in CoFeB and 2 × 10⁻³ in FeCo alloys were reported.^{28,29} From that moment, many groups^{3,23,24,30–35} have been synthesizing and studying Heuslers thin film compounds in order to implement them in devices (one can note that a large effort was done on that subject in Japan). Magnetic damping was thus explored in some Heuslers compounds and first found in the 10⁻³ range.^{28,36–40} Even if this was at least one order of magnitude higher than predicted ones, these results were very promising. Finally, it was not until recent years that we observed both full spin polarization and ultra-low magnetic damping in the 10⁻⁴ range close to the calculated ones,^{3,41,42} which makes these materials very promising for the future of spintronics and magnonics, especially in terms of energy consumption. As highlighted from *ab initio* calculations, some good HMM candidates belong to the Co₂YZ family with Y a 3d metal and Z a ns²np^{1–3} chemical element.^{4,7,9} Nonetheless, it took a long time to get both the minority spin gap and the ultra-low Gilbert damping as observed for some compounds in the Co₂MnZ family.^{3,35,41,43} We believe that this was due to the different issues encountered when growing thin films of Heusler compounds with such delicate properties. The first issue is obviously the structural quality. Nevertheless, it seems that Heusler compounds are very stable in their *m* $\bar{3}$ *m* point group structure, for many different chemical elements and deposition techniques such as ingot melting,¹² sputtering,^{24,31,35,44–46} molecular beam epitaxy (MBE),^{3,47,48} and pulse laser deposition.⁴⁹ But preparing these materials with the correct lattice is not sufficient. According to *ab initio* calculations,^{16,26,27,35} the correct chemical ordering in the lattice is crucial for getting expected electronic properties. Indeed, any chemical disordering, where a given crystallographic site is occupied by the wrong or more than one chemical element, may destroy the spin gap necessary to get low magnetic damping. The task is made difficult as several phases with different chemical orders are well known, although the cubic lattice is conserved, as shown in Fig. 1.⁵⁰

Starting from the original Heusler L2₁ phase (Cu₂MnSn prototype structure), the mixing of the different elements on the different crystallographic sites gives rise to the following phases: A2 (complete random disorder), B2 (Y/Z mixing), D0₃ (X/Y mixing), B32a (X₁/Z and X₂/Y mixing), and the inverse X phase, where one of the X atoms has swapped with the Y atom. Although the chemical disorder in the Heusler compound was studied experimentally^{33,35,51} and theoretically,^{26,27,35} its impact on the physical properties is not well understood and experimentally very difficult to quantify and disentangle from any other source of change, such as an off-stoichiometry for instance. Moreover, when chemical disorder is induced using ion irradiation,³³ there should also be structural defects induced as well. Finally, the characterization of the chemical ordering in thin films is often studied using x-ray diffraction, but we will see here that this technique using a single wavelength is not sufficient to distinguish several different phases possible in Heusler compounds. Consequently, there are two crucial issues to obtain Heusler compounds in thin films with the proper electronic properties. The first one is the stoichiometry that can be controlled up to a certain accuracy according to the growing process. The second one is the chemical ordering which is an intrinsic behavior and consequently not controllable when thermodynamic equilibrium is reached (by heating). One important conclusion of this paper is, on the one hand, to highlight the role of a very good control of the stoichiometry on the electronic properties (SP, spin gap, magnetic moment, and magnetic damping). On the other hand, the chemical ordering is studied in detail and its impact on observed electronic properties is discussed and compared to theoretical predictions. In the present work, we used molecular beam epitaxy (MBE) to grow Co₂MnZ epitaxial films on MgO(001) substrates. Indeed, the MBE technique has many advantages for testing the synthesis of new materials in thin films. First, the growth parameters can be set independently, such as the substrate temperature (*T*_{sub}), flux rates, and thickness of the film. Moreover, *in situ* characterization means are available, such as electron diffraction in real time or chemical surface analysis by x-ray or Auger spectroscopy after the growth process. Details on the epitaxial process of the films are given in Sec. II. In Sec. III, we show that the control of the atomic fluxes using quartz microbalances together with electron diffraction during the deposition allows us to estimate the control of the stoichiometry around ±1% for each element of the alloy. In Section IV, we show that the L2₁ Heusler phase in Co₂MnZ compounds cannot be claimed just by using standard electron or x-ray diffraction experiments. To address this point, scanning transmission electron microscopy combined with high angular dark field (STEM-HAADF) is performed. In Sec. V, the electronic properties of these compounds determined using magnetometry, photoemission, and ferromagnetic resonance are reviewed. A major result is the clear correlation between spin polarization and magnetic damping in Co₂MnAl_xSi_{1-x} quaternary alloys. Finally, we discuss the enormous potential of these alloys and the short-term challenges for spintronics.

II. EPITAXIAL GROWTH PROCESSES

A. Flux adjustment and control

The MBE system used is a COMPACT 21 EB 200 MBE system from RIBER with a base pressure equal to 3 × 10⁻¹¹ Torr (4 × 10⁻¹¹ hPa). This machine has been designed to be able to

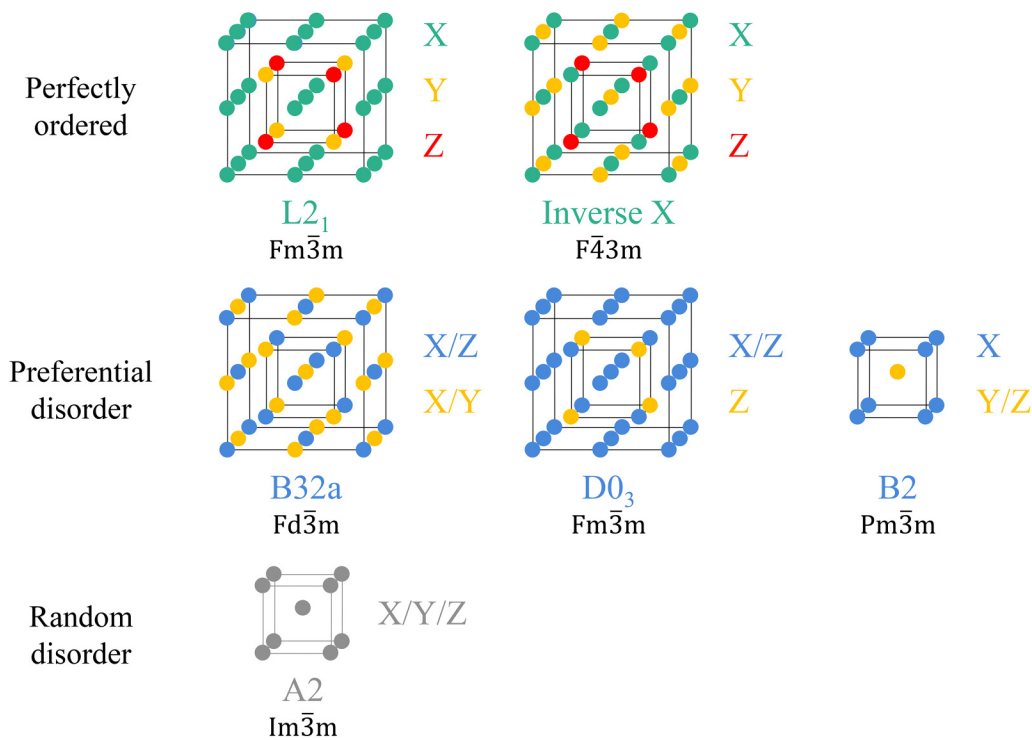


FIG. 1. Sketch of the different chemical ordering or disordering occurring in X_2YZ full Heusler compounds.

evaporate 24 chemical elements by using 3 multi-pocket e-guns (with 6 pockets each) and 6 Knudsen cells. Co_2MnZ layers with $Z = Al, Si, Ga, Ge, Sn,$ and Sb were deposited by the co-evaporation of each element with a precise control of the fluxes achieved with an INFICON IC6 controller (sensitivity 0.0004 nm) and four quartz microbalances (QMs), one QM for each e-gun and one additional QM to calibrate fluxes at the sample location. One should note that QM was preferred to other detection based on absorption, because a QM delivers an absolute measurement of the deposited mass (converted in growth rate) although absorption techniques need some reference samples. In this study, Co, Ge, Si, V, Cr, Au, and MgO were evaporated using e-guns and Mn, Ga, Sn, and Sb using Knudsen cells. The main benefit of using e-gun evaporation is the real time recording and regulation of the fluxes during deposition. This is achieved by using a feedback loop between the QMs and the high voltage power supply. For Knudsen cells, the flux stability is ensured by regulating the crucible temperature (leading to very stable flux over time). QMs are calibrated prior each deposition with the movable QM placed at the sample location. The cell fluxes were not measured in real time but calibrated using the sample QM before the deposition by fixing the cell temperature to get the correct growth rate. A sticking coefficient of 1 was first assumed at the surface of the QM and the sample for each element. It means that the surface density of atoms deposited on the quartz, in $at.cm^{-2}$, is equal to the one deposited on the sample, thus allowing a precise control of the layer thickness and stoichiometry. For the deposition of

Co_2MnZ epitaxial layer, the Co flux value was chosen equal to $10^{14} at.cm^{-2} s^{-1}$ and $\varphi_{Co} = 2\varphi_{Mn} = 2\varphi_Z$. The deposition rate V is linked to the flux via the equation, here given for Co,

$$\varphi_{Co} = V_{Co} \cdot n_{Co} = V_{Co} \cdot \frac{\rho_{Co} \cdot \mathcal{N}_A}{\mathcal{M}_{Co}}, \quad (1)$$

where n_{Co} is the volume density ($at./cm^3$), ρ_{Co} is the mass density (g/cm^3), \mathcal{M}_{Co} is the molar mass (g/mol), and \mathcal{N}_A is the Avogadro number ($at./mol$). It should be noted that the flux depends on the product of the growth rate and the mass density $V_{Co} \cdot \rho_{Co}$. To obtain the true growth rate on a QM, the mass density is needed. However, one can choose for a material an arbitrary mass density and fix the growth rate at a virtual value to get the chosen flux in Eq. (1). This is particularly interesting when growing alloys with several chemical elements that have to be calibrated separately, since the mass density of the compound can be chosen for all the elements of the alloy. Indeed, a Co_2MnZ Heusler film thickness is linked to the growth rates as

$$e_{CMZ} = \left(\frac{V_{Co}\rho_{Co} + V_{Mn}\rho_{Mn} + V_Z\rho_Z}{\rho_{CMZ}} \right) \cdot t_o = (V'_{Co} + V'_{Mn} + V'_Z) \cdot t_o, \quad (2)$$

where t_o is the deposition duration, V'_i is the virtual growth rate fixing the mass density of all i elements to the Co_2MnZ one (ρ_{CMZ}). For a Co_2MnSi film, using the molar masses M of each element as well as

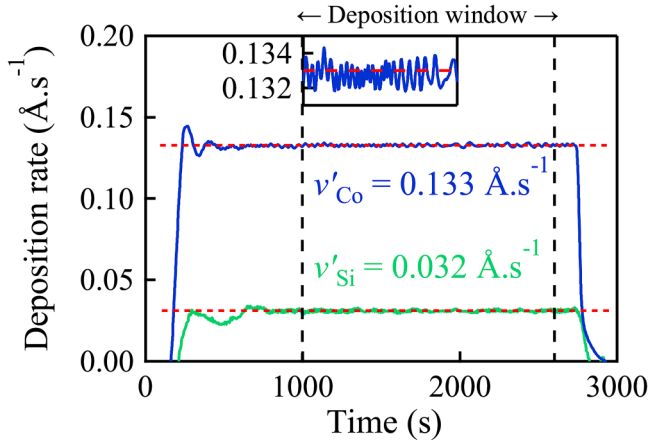


FIG. 2. Example of e-gun co-evaporated Co and Si growth rates measured by the QMs during the deposition of a Co_2MnSi epitaxial layer.

the density $\rho_{\text{Co}_2\text{MnSi}} = 7.4 \text{ g/cm}^3$, the growth rates that lead to $\varphi_{\text{Co}} = 2\varphi_{\text{Mn}} = 2\varphi_{\text{Si}} = 10^{14} \text{ at./cm}^2/\text{s}$ are

$$v'_{\text{Co}} = \frac{\varphi_{\text{Co}} \cdot M_{\text{Co}}}{\rho_{\text{Co}_2\text{MnSi}} \cdot N_A} = 0.133 \text{ \AA} \cdot \text{s}^{-1}, \quad (3)$$

$$v'_{\text{Si}} = 0.032 \text{ \AA} \cdot \text{s}^{-1}, \quad v'_{\text{Mn}} = 0.062 \text{ \AA} \cdot \text{s}^{-1}.$$

With those rates, it takes 6.25 s to grow one Co_2MnSi atomic plane (12.5 s for two planes, 25 s for one unit cell). An example of e-gun fluxes regulation during a deposition of Co_2MnSi is presented in Fig. 2. Both curves were recorded with a 10 s rate filter (the growth rate is measured every 0.1 s and averaged over the past 10 s). The typical instantaneous set point deviations were smaller than 3%, as shown in the inset of Fig. 2, and integration over time smaller than 0.5%. For the Knudsen cells, the flux stability is ensured by the crucible temperature regulation ($\pm 0.2 \text{ }^\circ\text{C}$) with a better accuracy than with an e-gun, so a real time control of the cell flux is not necessary.

B. Substrate and buffer layer choice

To get epitaxial Heusler thin films, single-crystalline MgO (001) substrates were used. MgO substrates were outgassed *in situ* at around $800 \text{ }^\circ\text{C}$. A MgO buffer layer was systematically deposited at around $750 \text{ }^\circ\text{C}$ in order to smooth the surface and burry contaminants underneath.⁵² The Co_2MnZ films with $Z = \text{Al, Si, Ga, Ge, Sn, and Sb}$ were first deposited on MgO^{3,41} and epitaxial growth was obtained at $T_{\text{sub}} \sim 450 \text{ }^\circ\text{C}$, except for Co_2MnSb . Due to competition between surface and interface energies,⁵³ the growth mode of all Heusler films on MgO is three-dimensional. The film thicknesses were thus chosen in the range of 20–30 nm to get coalesced and continuous thin films. The films were heated up to $T_{\text{sub}} \sim 750 \text{ }^\circ\text{C}$ after growth to get the chemical ordering at thermodynamic equilibrium. The films were capped with 2 to 10 nm Au films to protect them from air. Another possibility is to grow these films on a metallic buffer layer for which a layer by layer growth mode is

possible. This process has three major advantages. First, epitaxial Co_2MnSb films were only obtained on such a V buffer layer. Second, very thin continuous films may be grown (1 atomic plane thick is possible). Third, the Heusler film growth rate can be measured very precisely using electron diffraction as explained in the next section. Hence, the Co_2MnZ films growth was also tested on V(001) epitaxial buffer layers. This choice is motivated first because the intermixing temperature of metals in V is usually large, and second, because the V lattice parameter is close to MgO and Co_2MnZ Heusler compounds. 20 nm thick V buffer layers were first grown at room temperature and annealed around $700 \text{ }^\circ\text{C}$ to get a smooth surface.⁵⁴ The Co_2MnZ films were thus epitaxially grown around $250 \text{ }^\circ\text{C}$ (in order to get RHEED oscillations) and annealed after the growth up to $550 \text{ }^\circ\text{C}$ (V and Co_2MnGa intermixing was observed to take place above $700 \text{ }^\circ\text{C}$, as checked by Auger spectroscopy). Typical reflection high energy electron diffraction (RHEED) patterns of the prepared MgO, V buffer layers, and Co_2MnZ films are presented in Fig. 3. All the RHEED patterns were showing thin and smooth streaks, indicating excellent surfaces quality with large crystallographic terraces. Kikuchi lines are visible on MgO RHEED patterns, typical of very clean and well oriented MgO surfaces.⁵⁵ The RHEED patterns of the V surface were compatible with a pure surface without detectable contamination.⁵⁴ The epitaxial relationship between V and MgO, and Co_2MnZ and V, is given in Fig. 3. Note that the cubic V unit cell is 45° turned compared to MgO one, since the misfit is close to zero in this case [$a_{(110)}(\text{MgO}) = 0.298 \text{ nm}$ and $a_{(100)}(\text{V}) = 0.303 \text{ nm}$]. The Co_2MnZ and V layers are cube on cube oriented. Note that the misfit with V is thus not always small and may lead to strain in the selected Z-based Heusler film. Indeed, if the misfit is close to zero for $Z = \text{Sn}$ ($a_{(200)}\text{Co}_2\text{MnSn} = 0.300 \text{ nm}$), it can reach 4% for $Z = \text{Si}$ ($a_{(200)}\text{Co}_2\text{MnSi} = 0.283 \text{ nm}$). Some tetragonalization of the cubic unit cell for Co_2MnZ films was actually observed. To eliminate the strain, the Heusler films can also be grown on BCC Cr buffer layers ($a_{(100)}\text{Cr} = 0.288 \text{ nm}$). Similar RHEED patterns were observed using Cr buffer layers.

III. STOICHIOMETRY CONTROL

The stoichiometry of our films is strongly dependent on the hypothesis of full sticking of the atoms on the quartz and on the sample (sticking coefficient = 1). We used two complementary methods to evaluate this hypothesis and thus to test the stoichiometry of the films, one by measuring the film thickness after the growth using x-ray diffraction and the other by measuring the time to complete a layer during the growth using electron diffraction.

A. Stoichiometry checking by thickness measurement

The basic argument is to consider that a correct control of fluxes may lead to a calculable film thickness after a fixed deposition time that can be compared to thickness measurement. The expected thickness is given by Eq. (2). It should be noted that the Co_2MnZ mass density is needed to fix the different growth rates using Eq. (1). The thicknesses were thus checked after the growth using x-ray reflectivity (XRR) measurements, the mass density using the lattice parameters given by (001) diffraction diagrams at large angles,⁴¹ and the molar mass of the primitive lattice considering a perfect stoichiometry. The thickness test was performed on the

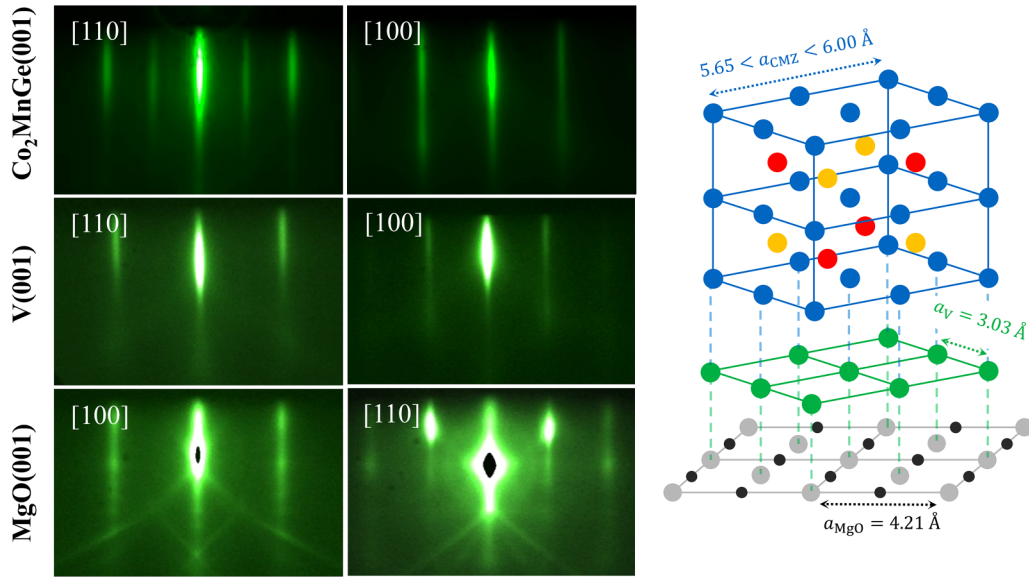


FIG. 3. (Left) Typical RHEED patterns of the MgO substrate, V buffer layer, and Co₂MnZ films (here Z = Ge) and right is the sketch of the epitaxial relationships between the layers.

Co₂MnZ films grown with $\varphi_{\text{tot}} = 2 \times 10^{14}$ at. cm⁻² s⁻¹. Since at the very beginning of growth tests, we do not know several parameters (such as the lattice spacing) to fix the film thickness, we stopped the growth when a virtual Co thickness $e'_{\text{Co}} = v'_{\text{Co}} t_o = 10$ nm in Eq. (2) was reached on the Co QM measurement during the CMZ film deposition. The deposition time is thus $t_o = e'_{\text{Co}}/v'_{\text{Co}}$ and the total thickness is calculated using Eqs. (1) and (2) as

$$e_{\text{CMZ}} = e'_{\text{Co}} \left(1 + \frac{v'_{\text{Mn}} + v'_{\text{Z}}}{v'_{\text{Co}}} \right) = e'_{\text{Co}} \left(1 + \frac{M_{\text{Mn}} + M_{\text{Z}}}{2 \cdot M_{\text{Co}}} \right) = e'_{\text{Co}} \cdot A. \quad (4)$$

It should be noted that the A factor is not equal to 2 in general. $A = 2$ if the average mass of Mn and Z is equal to Co mass which is almost the case for Co₂MnGa, but $A = 1.7$ for Co₂MnAl. The XRR spectra of the films directly grown on MgO are presented in Fig. 4 together with their best fits. In Table I are reported the expected thicknesses compared to the XRR measurement. The case of Co₂MnSb grown on a V buffer layer is discussed in the next section.

The measured thicknesses are in very good agreement with the calculated ones. This confirms the assumption on unity sticking coefficient on the QM and on the sample during growth. The film thickness determination is thus a first test to control the compounds composition. However, the accuracy on the stoichiometry is not better than 5% essentially due to the error bar on the thickness determination using the fits. We will see in the next section that electron diffraction helps to better control it.

B. Real time measurement of Heusler growth rate

A MBE machine is usually equipped with electron diffraction facilities, especially reflection high energy electron diffraction—

RHEED. This is a powerful technique which gives in real time the epitaxial relationship of the deposit with respect to the single-crystalline substrate.⁵⁶ But more interestingly, RHEED intensity oscillations are usually observed if a layer-by-layer growth process

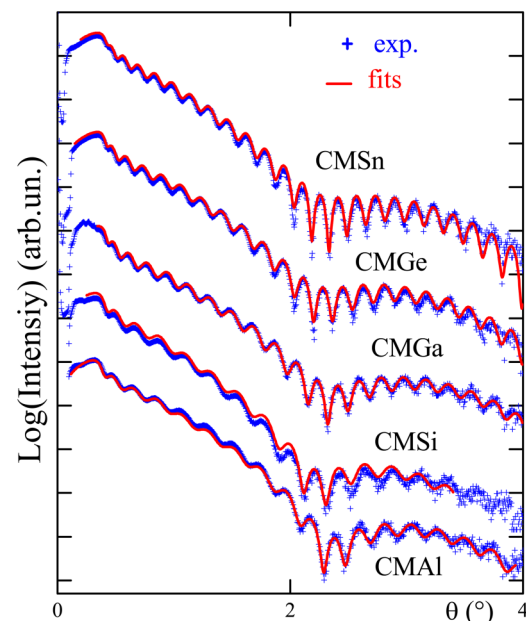


FIG. 4. XRR spectra and associated fit for a series of Co₂MnZ Heusler compounds directly grown on MgO. The fitting parameters are given in Table I.

TABLE I. Comparison between calculated thicknesses considering Eq. (4) with $e_{\text{Co}} = 10$ nm and thicknesses determined by fitting the XRD spectra in Fig. 4.

	A factor	Thickness (nm)	
		Calculated (± 0.5 nm)	Measured (± 1 nm)
Co ₂ MnAl	1.7	17.0	17.7
Co ₂ MnSi	1.71	17.1	17.3
Co ₂ MnGa	2.06	20.6	21.2
Co ₂ MnGe	2.08	20.8	22.5
Co ₂ MnSn	2.47	24.7	24.9

occurs.⁵⁷ The period of an oscillation is thus equal to the time delay to complete one or two atomic layers, which is a very nice tool to measure in real time the compound growth rate and consequently to control the stoichiometry. An example of RHEED intensity oscillations during the deposition of Co₂MnSn compounds at $T_{\text{sub}} = 200$ °C on top of a V buffer layer is presented in Fig. 5. A small window is selected on a RHEED streak (usually the central one) and the intensity recorded during the growth presents clear oscillations. The corresponding Fourier transform gives a frequency equal to 0.0907 Hz which gives a 11.0 s period. According to the flux choice [Eq. (1)] and the lattice spacing equal to 0.599 ± 0.001 nm in

our Co₂MnSn films,⁴⁰ the theoretical time to grow one atomic plane is equal to 5.55 s, so 11.1 s for a double atomic plane period. Thus, the observed period corresponds to the completion of two atomic planes. It means that the growth of Co₂MnSn is bilayer by bilayer. This bilayer growth process is also observed on the other Co₂MnZ compounds on V or Cr buffer layers at 200 °C. The calculated time to grow a bilayer can be calculated using Eqs. (1) and (2) as

$$T_{\text{CMZ}} = \frac{a_{\perp}}{2} \cdot \frac{\rho_{\text{CMZ}}}{\varphi_{\text{tot}}} = \frac{8}{a_{\parallel}^2 \cdot \varphi_{\text{tot}}}, \quad (5)$$

where ρ_{CMZ} is here the atomic density, a_{\perp} is the lattice parameters along the growth axis, and a_{\parallel} the in-plane lattice spacing. We chose buffer layers with appropriate small misfit to get small strain ($a_{\text{Cr}} = 0.288$ nm and $a_{\text{V}} = 0.303$ nm). We thus consider bulk lattice spacing of the Heusler compounds to calculate the expected period. The comparison with RHEED oscillations measurement is shown in Table II. The error bars on the calculated periods are due to the uncertainty on the lattice spacing (± 0.001 nm) and on the total flux ($\pm 3\%$). The accuracy of the experimental oscillations frequency is given by the width of the FT peak which did not exceed 2%. The agreement between calculation and experiment is excellent and validates our calibration process.

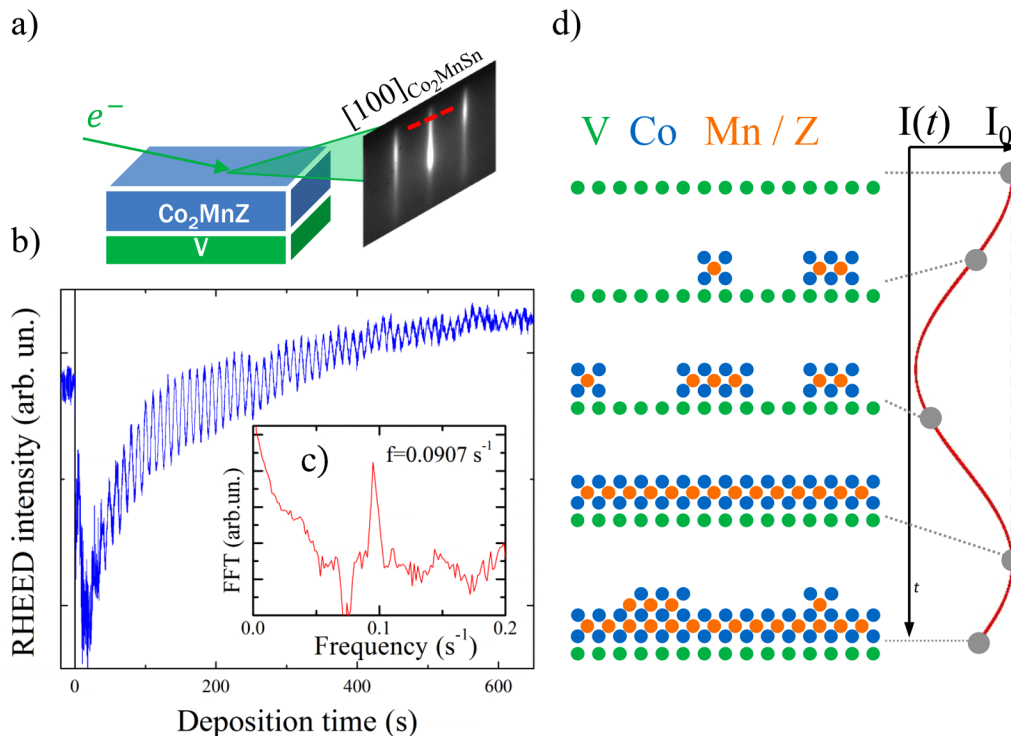
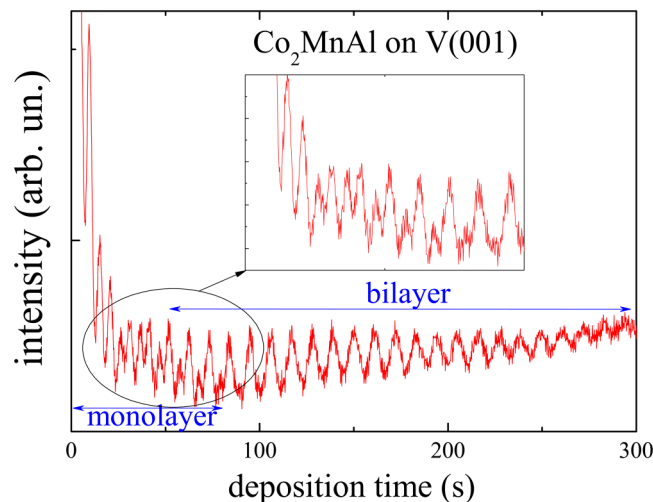


FIG. 5. (a) Section of the central line intensity in the [100] azimuth of Co₂MnSn recorded over time, (b) the intensity line profile, showing clear oscillations, (c) corresponding Fourier transform indicating a frequency $f = 0.0907$ Hz, (d) sketch explaining the bilayer growth mode together with the intensity on the RHEED screen.

TABLE II. Comparison between expected times to complete a bilayer calculated using the flux calibration and RHEED oscillation periods.

	Buffer	a_{CMZ} (nm)	Calculated period (s) $\pm 4\%$	Observed period (s) $\pm 3\%$	Diff. (%)
Co ₂ MnAl	Cr	0.574	12.14	12.0	-1.1
Co ₂ MnSi	Cr	0.566	12.49	12.45	~0
Co ₂ MnGa	Cr	0.575	12.1	11.6	-4.1
	V	0.575	12.1	12	-0.8
Co ₂ MnGe	Cr	0.576	12.05	12.0	~0
Co ₂ MnSn	V	0.599	11.15	11.0	-1.3
Co ₂ MnSb	V	0.592	11.41	11.4	~0

The bilayer growth mode is well-known for MBE-grown semiconductors^{58,59} and is associated to the covalent tetrahedrons stability, which are the basic blocks of the zinc blend or diamond structures. Similarly, the basic block for Co₂MnZ Heusler compounds is a cube with Co atoms at its eight corners, and Mn or Z in the center of the cube (see Fig. 1). These Heusler compounds thus want to develop these basic blocks during the growth, leading to bilayer growth as sketched in Fig. 5 with the corresponding RHEED intensity oscillations. *This bilayer growth is a strong demonstration of these Heusler compounds' stability and their natural trend for chemical ordering*, at least between Co and Mn/Z atoms. As in semiconductors, this bilayer process is sensitive to the growth temperature. Indeed, similar RHEED experiments were performed at room temperature and oscillations corresponding to one atomic plane were sometimes observed at the beginning of the growth as shown in Fig. 6 in the case of Co₂MnAl on V. After some few atomic planes grown, this monolayer growth process is replaced by

**FIG. 6.** RHEED oscillations obtained during Co₂MnAl growth on V(001) at room temperature: a monolayer growth was observed at the beginning of the growth, and a transition to a bilayer growth took place after around 10 atomic planes. This monolayer regime was not observed for substrate temperatures above 200 °C.

the bilayer growth process. This transition means that the chemical ordering did not occur at the beginning of the growth where the surface contains large terraces. The transition from monolayer to bilayer growth may be explained by the increase in the density of steps during such out-of-equilibrium growth process, as well-known in MBE.⁵⁶ This transition between monatomic to bilayer growth process was observed to strongly depend on the substrate temperature and is suppressed above $T_{\text{sub}} = 200$ °C. The ultimate test of the stoichiometry is to perform both *in situ* electron diffraction and *ex situ* thickness control. The example of the Co₂MnGa film deposited on a V buffer layer is shown in Fig. 7. The film was grown on V during $t_0 = 650$ s. According to Eqs. (1) and (2), the expected Co₂MnGa thickness was 15.55 nm and the period of a bilayer growth equal to 12.09 s. As shown in Fig. 7, the RHEED oscillations FFT gives $f = 0.0833$ Hz leading to a period equal to 12.00 s, and the reflectivity curve fit gives a thickness equal to 15.6 ± 0.1 nm. Using both techniques, the deviation between calculations and measurements is around 1%.

IV. CHEMICAL ORDERING IN HEUSLER EPITAXIAL FILMS

A. X-ray diffraction

XRD was first used to determine the chemical ordering in our Heusler layers, using a D8 Advance Bruker diffractometer for the symmetrical configuration and the 4-circles MRD PANalytical diffractometer for the asymmetrical reflections. We extracted first the lattice spacing by measuring the XRD diagram along (00 l) as shown in Fig. 8. The lattice spacing extracted from these XRD spectra is compared to *ab initio* calculations, bulk and thin film measurements reported in the literature (Table III). The very similar values between calculation and experiments show first that theory is able to account for experimental results. Second, the similarity between bulk and thin films is another indication of the good control of the stoichiometry in our films. On the other hand, the lattice spacing dependence with the covalent radius of the Z element is plotted in Fig. 9. A linear variation is observed, which strongly supports that Co₂MnZ crystals do not bind as full metals but are hybrid materials, in between metals and covalent solids.

One should note that the epitaxial growth direction of the Au capping differs from one Heusler film to the other. As a (001) epitaxial growth is expected due to the small misfit between the [100] Heusler spacing and the [110] FCC Au lattice spacing, a (111) growth is observed for Co₂MnSi and Co₂MnGe. We have no explanation for that behavior and this is not the aim of the paper to address this point. Nevertheless, the Au capping films were observed to wet the Heusler films ensuring their protection from air (see the next section). The (00 l) XRD diagrams are not sufficient to get the chemical ordering. Moreover in several experimental studies,^{24,43,65,66} the L₂₁ structure is claimed by observing (111) or (311) reflections. We demonstrate in this section that it is not so straightforward. One elegant way to calculate the diffracted peak intensities depending on the chemical ordering is to consider the four different sites noted α , β , γ , and δ in the basic cubic structure¹² as shown in Appendix A. The structure factor $F(h, k, l)$ is thus calculated considering the scattering on each site. To get these factors for

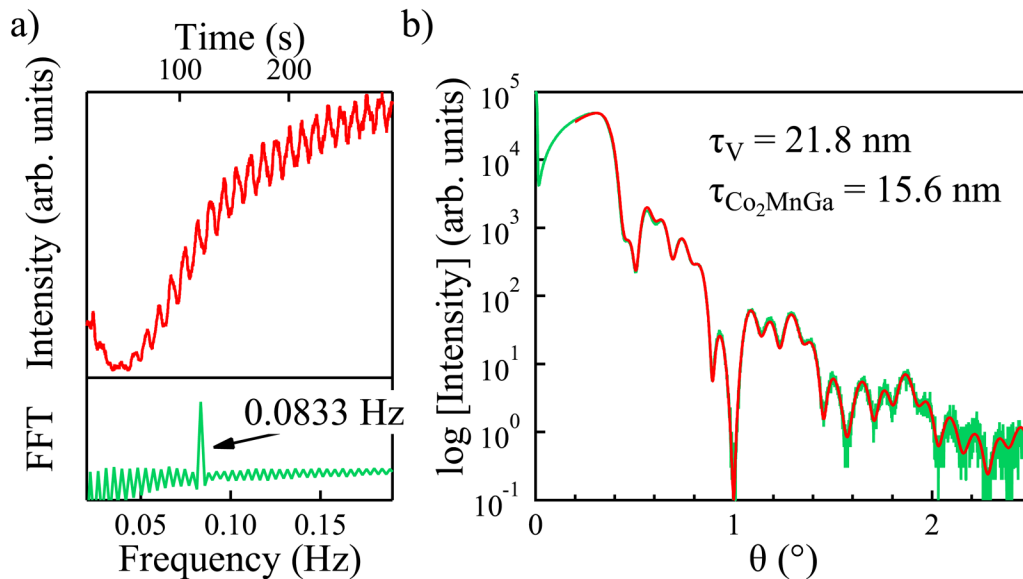


FIG. 7. Test of the stoichiometry on a Co_2MnGa film grown on V by performing both RHEED oscillations (a) and x-ray reflectivity (b)—see text.

the structures described in Fig. 1, each atom has to be affected on one site. Using this method, the structural factors per X_2YZ unit formula are calculated as a function of the atomic scattering factors f_x , f_y , f_z for each possible structure as shown in Table IV.

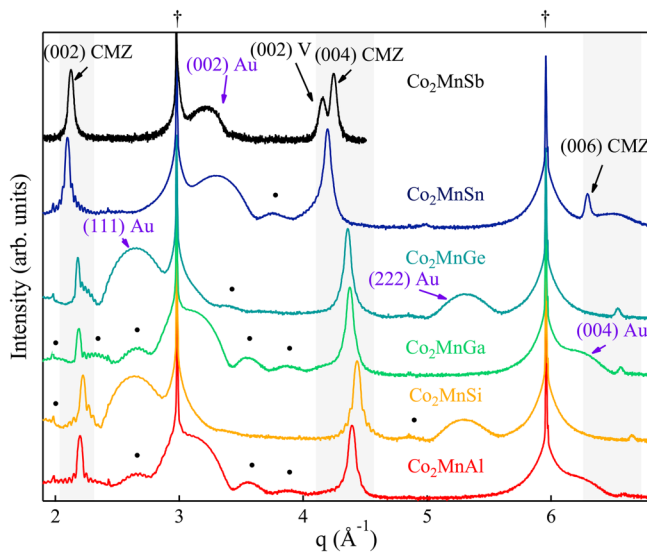


FIG. 8. XRD spectra of Co_2MnZ Heusler thin films. Co_2MnZ peaks are labeled as (002), (004), and (006). Peaks labeled as † are from the MgO substrate. The • marks correspond to the Kiessig oscillations around the (111) or (001) peaks from the 2 nm thick Au capping.

We analyzed in detail (311), (222), and (111) peaks corresponding, respectively, to $h+k+l = 4n+1$, $4n+2$, and $4n+3$ diffraction conditions for the Co_2MnZ series as shown in Fig. 10 [except $Z = \text{Sb}$ where we measured only the (111) peak and not the others]. At this point, the observation of (222) peaks indicates that A2 and B32a phases are excluded in our films. The observations of (111) and (113) peaks indicate that the B2 phase is also excluded except for Co_2MnAl (as reported in the literature¹²). For the other compounds, there are no further indications on which phase between $L2_1$, $D0_3$, and inverse X takes place.

A quantitative analysis of the Co_2MnZ XRD reflections intensities (proportional to the square of the structural factor) is thus necessary (see, for instance, Ref. 67) However, we did not succeed in determining the chemical ordering in these particular Co_2MnZ compounds using regular XRD because Co and Mn scattering factors are very close to each other.⁶⁸ Indeed, the structure factors

TABLE III. Comparison of Co_2MnZ lattice spacing obtained by *ab initio* calculations, in the bulk, and in thin films. The error bar on the lattice spacing values in this work was extracted from many samples measurement.

	Lattice spacing (nm)			
	Theory ⁶⁰	Bulk ¹²	Thin films	
			This work (± 0.001 nm)	Others
Co_2MnAl	0.573	0.576	0.574	0.578 ⁶¹
Co_2MnSi	0.563	0.565	0.566	0.5645 ³⁸
Co_2MnGa	0.573	0.577	0.575	0.579 ⁶²
Co_2MnGe	0.574	0.574	0.576	0.577 ⁶³
Co_2MnSn	0.598	0.600	0.599	0.600 ⁶⁴
Co_2MnSb	0.601	0.593	0.592	...

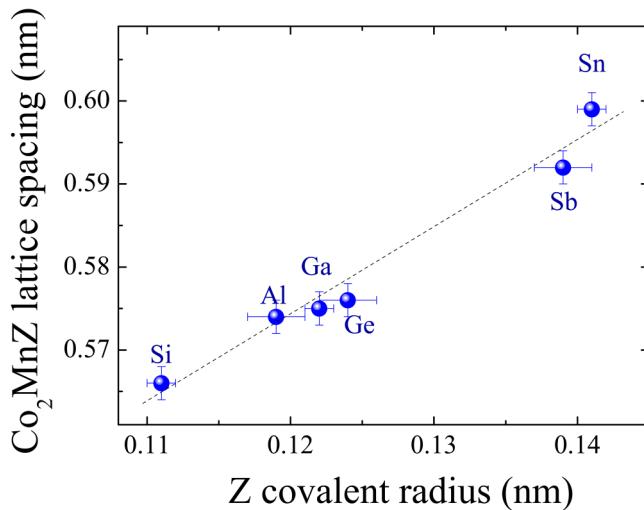


FIG. 9. Lattice spacing dependence upon covalent radius Co₂MnZ thin films. The dashed line is here to guide the eyes.

for $h + k + l = 4n$ or $4n + 1$ or $4n + 2$ are similar by considering $f_X \approx f_Y$ (see Table IV),

$$F_{Co_2MnZ}^{L2_1} \cong F_{Co_2MnZ}^{D0_3} \cong F_{Co_2MnZ}^X \cong f_Z - f_Y. \quad (6)$$

This clearly means that one cannot distinguish easily between these three structures in these Co₂MnZ compounds by comparing diffracted peak intensities using regular x-ray diffraction. This is an important conclusion since the L₂₁ chemical ordering in Co₂Fe- or Co₂Mn-based Heusler compounds is claimed in a lot of papers^{34,44,69–71} based on the observation of (111), (222), or (113) XRD peaks. Anomalous x-ray diffraction is thus absolutely necessary to overcome this problem and sometime used,^{72–74} but it requires a synchrotron source. Finally, Co₂MnSb cannot be described by none of these chemical ordering. Indeed, its (002) and (004) diffraction peaks have similar intensities that contrast with

the other compounds (Fig. 8) and with results in Table IV. Even if its lattice is also FCC as the others, we have no information about the chemical ordering in the Co₂MnSb lattice. To summarize, among all the possible chemical ordering in the Heusler FCC cell, regular XRD allowed us to eliminate the A2 and B32a structures in our films. The B2 structure is confirmed in Co₂MnAl thin films. Nevertheless, XRD did not allow us to distinguish between the L₂₁, D0₃, and X phases in the other Heusler films studied here, and none of these structures allow us to describe the chemical ordering in Co₂MnSb. To obtain this information, the use of ultra-high resolution transmission electron microscopy was preferred since this technique also provides spatial resolution.

B. Transmission electron microscopy

The Co₂MnZ series was analyzed by scanning transmission electron microscopy (STEM). In particular, the high angular annular dark field (HAADF) mode detection was used due to the low contrast between the chemical elements in the compounds, such as Co, Mn, Ge, and Ga. HAADF is a detection method where electrons scattered at high angles are collected by an annular detector located around the incident beam. Since heavy elements scatter electrons much more than lighter ones, the brightness on HAADF images indicates heavy elements, whereas darkness indicates light elements. The STEM-HAADF investigation was carried out using a JEM—ARM 200F Cold FEG TEM/STEM, operating at 200 kV and equipped with a spherical aberration probe and image corrector. A point resolution of 0.78 Å in the STEM mode is reached on this setup. 50–60 nm thick cross sections were prepared along the Co₂MnZ [110] zone axis by focused ion beam etching using Ga ions. The [110] zone axis is very suitable to study chemical disorder in Heusler compounds since it has only mono-elemental columns at least for the L₂₁ and inverse X structures, as shown in Fig. 11. Thus, very different patterns should be observed depending on the chemical ordering, especially when the contrast is high between Z and Mn atoms, for instance, in Co₂Mn-Al, -Si, -Sn, and -Sb. For the two other compounds (-Ge and -Ga), the contrast is low and the chemical ordering is thus difficult to see by the eyes. In that case, profiles along [110] and [001] azimuths help to determine the structure.

TABLE IV. Intensity of the possible diffracted peaks according to the different chemical ordering in the X₂YZ Heusler cells described in Fig. 1 (see Appendix A).

h,k,l same parity	Intensity dependence for X ₂ YZ Heusler structures					
	A2	B2	B32a	D03	L ₂₁	X
$h + k + l = 4n$ (004) (220)				$ 2f_X + f_Y + f_Z ^2$		
$h + k + l = 4n + 1$ (113) (135)	0	0	$ f_Z - f_Y ^2$	$ f_Z - \frac{2}{3}f_X - \frac{1}{3}f_Y ^2$	$ f_Z - f_Y ^2$	$ f_Z - f_Y ^2$
$h + k + l = 4n + 2$ (002) (222)	0	$ 2f_X - f_Y - f_Z ^2$	0	$ \frac{2}{3}f_X + \frac{1}{3}f_Y - f_Z ^2$	$ 2f_X - f_Y - f_Z ^2$	$ f_Z - f_Y ^2$
$h + k + l = 4n + 3$ (111) (133)	0	0	$ f_Z - f_Y ^2$	$ f_Z - \frac{2}{3}f_X - \frac{1}{3}f_Y ^2$	$ f_Z - f_Y ^2$	$ f_Z - f_Y ^2$

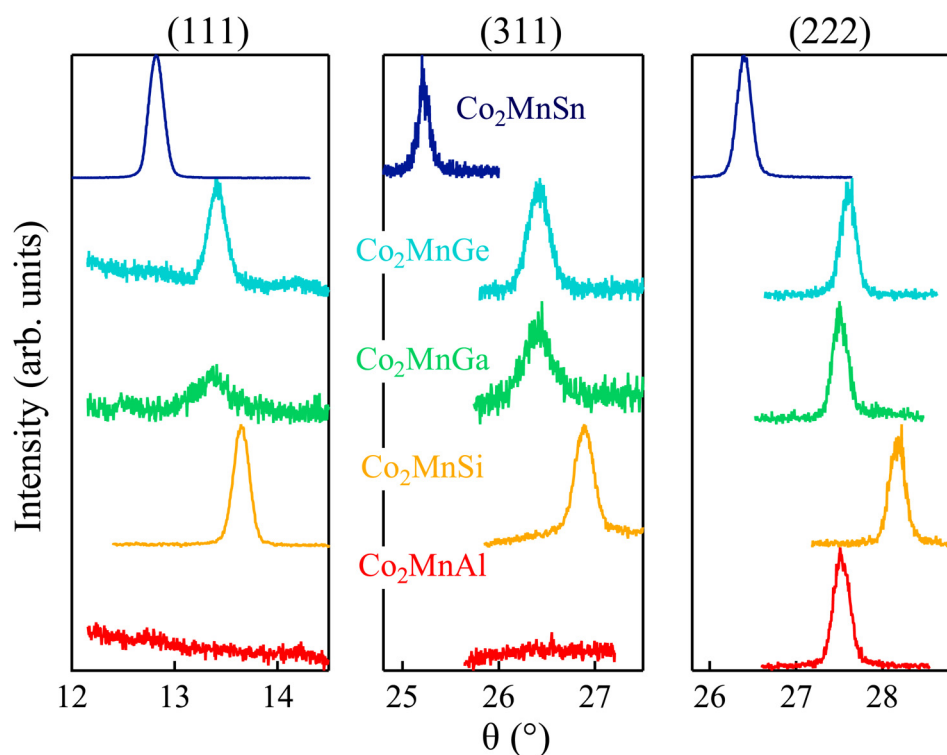


FIG. 10. XRD diagrams around (111), (311), and (222) for the Co_2MnZ series.

The STEM-HAADF micrographs and intensity profiles are first shown for Co_2MnSi , Co_2MnGa , and Co_2MnGe in Fig. 12. Beside the fact that these three films have an excellent crystalline quality, the different intensity profiles demonstrate the $L2_1$ structure in these compounds. Indeed, intensity profiles along [001]

indicate the vertical Z–Co–Mn–Co–Z column sequence. Two kinds of profiles were observed along [110], one corresponding to a series of Co columns and the other to a periodic sequence of Mn–Z columns. This is exactly what is expected for the $L2_1$ chemical ordering (Fig. 11).

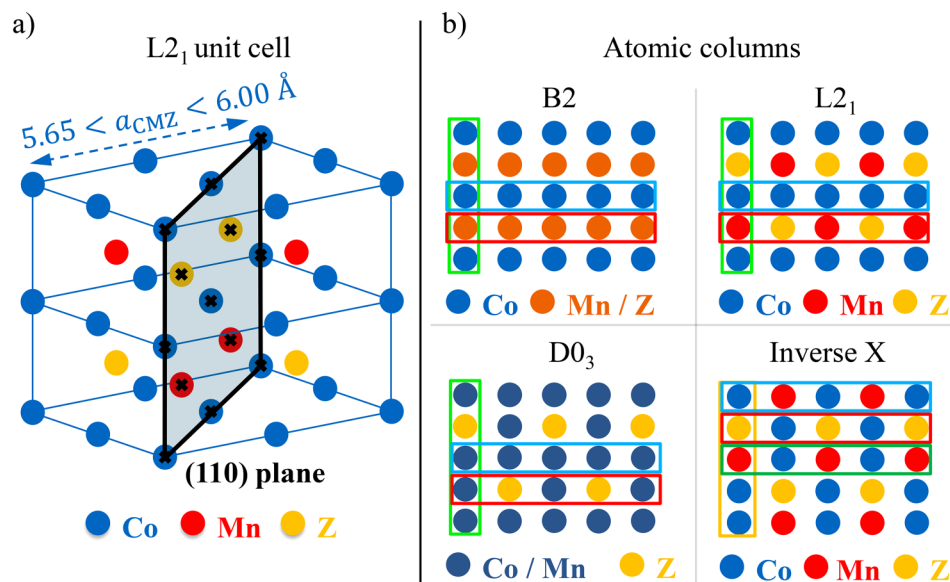


FIG. 11. (a) Schemes of the [110] zone axis in the Heusler structure and (b) atomic columns for the four possible structures delimited by x-ray diffraction. The different profiles that allow us to distinguish between the four structures are also shown.

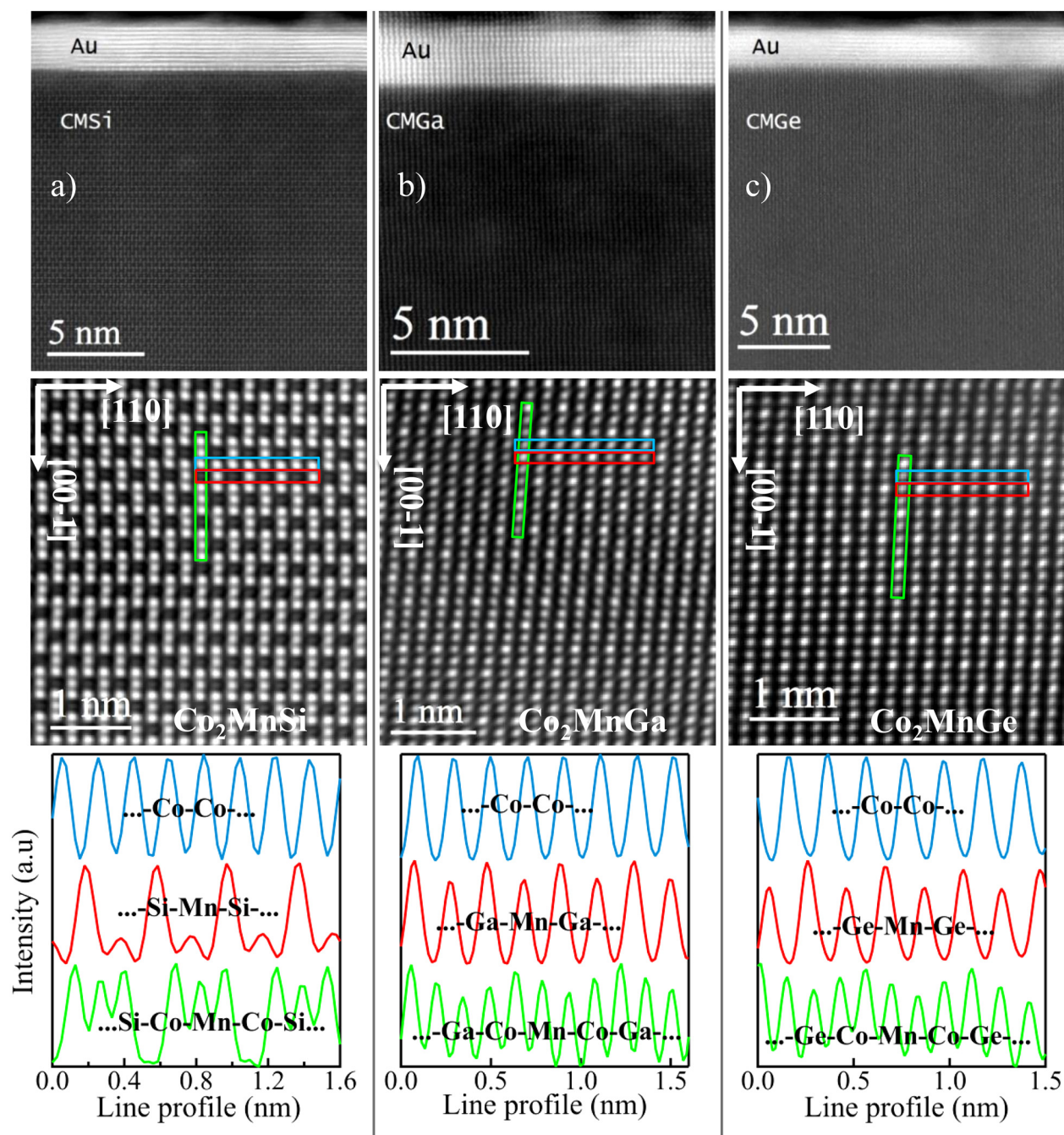


FIG. 12. STEM-HAADF micrographs and intensity line profiles of Co_2MnZ compounds with $Z = \text{Si}$ (a), Ga (b), and Ge (c). The profiles along $[110]$ and $[001]$ allow us to identify a $L2_1$ chemical ordering for these compounds.

As expected according to RHEED and XRD results, this $L2_1$ chemical ordering is not observed on Co_2MnAl and Co_2MnSb micrographs, but more surprisingly also not on Co_2MnSn . For Co_2MnAl , we have seen by RHEED and XRD that a B2 phase was

occurring, which is a random mixing of Mn and Al on their sites. This is what we observed since the $[110]$ atomic columns in Fig. 13(a) actually correspond to the B2 pattern in Fig. 11. The situation is quite different for Co_2MnSn . If in some places of the

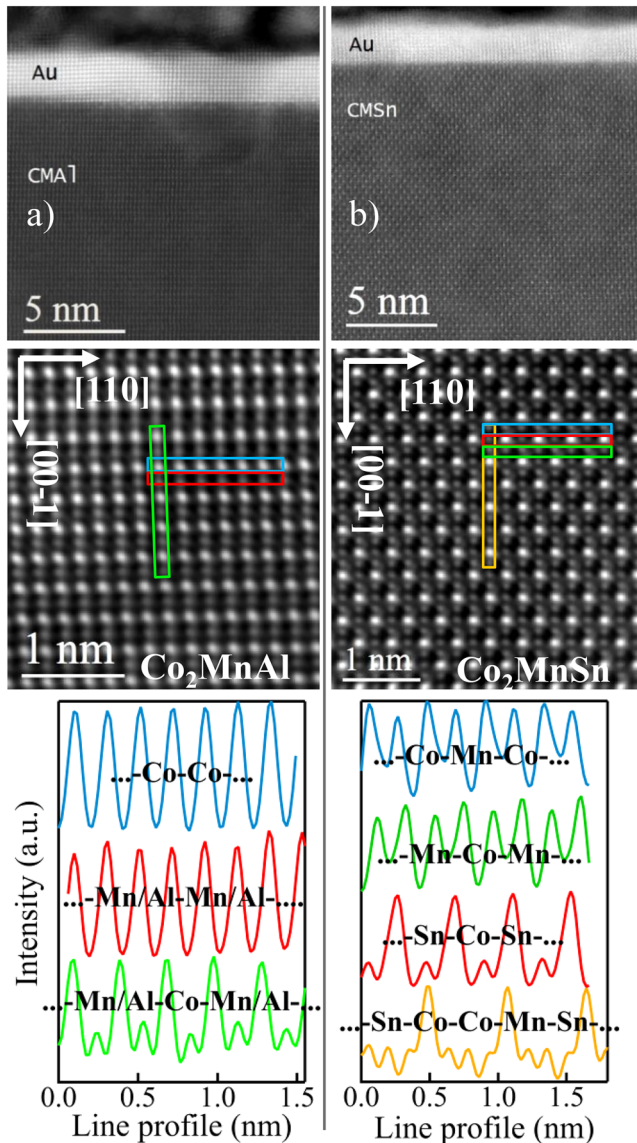


FIG. 13. STEM-HAADF micrographs and intensity line profiles of (a) Co_2MnAl and (b) Co_2MnSn compounds. The profiles along $[110]$ and $[001]$ allow us to confirm the B2 structure for $-\text{Al}$. For the $-\text{Sn}$ compound, a mixing of $L2_1$ (not shown) and inverse X (shown here) was observed.

cross section, a $L2_1$ ordering was observed (not shown here), an inverse X phase pattern was also observed as shown in Fig. 13(b). One site of Co and the site of Mn have swapped, leading to the $[110]$ columns distribution as sketched in Fig. 11 for the inverse X structure (see Fig. 1). Our Co_2MnSn films are thus made of a mixing of $L2_1$ and inverse X chemical orderings. Finally, if the Sb location was clearly visible on Co_2MnSb micrographs as in Co_2MnSn , the profile analysis did not allow us to identify any chemical ordering on the sites around Sb (not shown see,

Ref. 68). The chemical ordering is thus still an open question for Co_2MnSb , but a mixing of phases ($\text{CoMnSb} + \text{Co}_2\text{MnSb}$) has to be considered, as proposed in the bulk.¹² Finally for all the compounds, the Au capping layer has grown epitaxially with very smooth and flat interfaces, either (001) for $Z = \text{Al, Ga, Sn}$ or (111) for $Z = \text{Si and Ge}$, as already shown by XRD in Fig. 8. This is promising for future stack designs using Au-spacer based spin valves. It should be noted that we also used Ag for capping, but a 3D growth on Co_2MnGe was clearly identified using similar STEM analysis. One should take care about using Ag as a spacer in Co_2MnZ Heusler-based spin valve devices, at least when using MBE as the growth process.

V. ELECTRONIC PROPERTIES IN CO_2MnZ HEUSLER THIN FILMS

Using *ab initio* calculations, some specific features were predicted for this Co_2MnZ Heusler family (Table V). First, the spin polarization near the Fermi energy was predicted to be 100% for some of these Heusler compounds, but not for all. Second, the magnetic moments per unit formula were determined for each element in the compounds, and the average moment per unit cell was found to be governed by the Slater-Pauling behavior.⁶ Third, ultra-low magnetic damping coefficients were calculated.^{27,75}

In the following, a review of experimental magnetic properties reported in previous papers^{3,41,42,68} but also new results are given. Appropriate techniques such as spin-resolved photoemission spectroscopy (SR-PES), x-ray magnetic circular dichroism (XMCD) (both performed at SOLEIL synchrotron sources) and ferromagnetic resonance (FMR) were used. In the first section, we first show that FMR is a very powerful tool to control the quality of Heusler compounds and hence help us to get ultra-low magnetic damping. In the second section, an experimental review of our reported results is proposed and compared to theoretical expectation of Table V.

A. FMR: A powerful tool to study Heusler compounds

An FMR analysis gives many parameters, i.e., absolute magnetic moment, anisotropy, Landé factor, and magnetic damping, noted α in the following (see Appendix B). This technique is also extremely sensitive to any defects in the films. In many experimental papers, unexpected results are discussed considering chemical disordering. But another feature to explore is the influence of some deviation from stoichiometry on the electronic properties. Such a deviation may lead to areas of chemical disorder that can be detected by FMR, even if most of the material is in a perfect (here cubic) structure. We, therefore, first looked at the effect of a deviation from the 2:1:1 stoichiometry on the ferromagnetic resonance spectra. Second, we investigate the FMR response on Heusler films containing two different chemical orderings. Third, we looked at the FMR response of Heusler polycrystalline films with structural disorder at grain boundaries. A series of off-stoichiometric $\text{Co}_{2-x}\text{Mn}_{1+y}\text{Si}_{1+z}$ films were prepared with $x = y + z$ (to respect the total number of 4 atoms in the primitive cell) and were examined by FMR. The stoichiometry was achieved by using the flux calibration process with the help of a QM as described in Sec. III. A vector network analyzer ferromagnetic resonance (VNA-FMR) setup was

TABLE V. theoretical prediction of spin polarization, magnetic moment (per Co_2MnZ unit formula) with Slater–Pauling expectation, and magnetic damping for the Co_2Mn -based Heusler series (see Ref. 41).

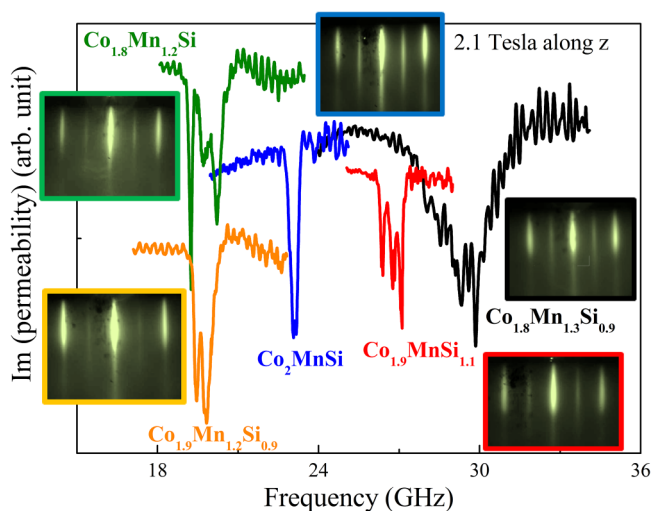
	Predicted structure	Calc. spin polarization (%)	Calc. magnetic moment (μ_B) ^{6,8}	Slater–Pauling (μ_B)	Calc. magnetic damping
Co_2MnAl	B2	68	3.97	4	
Co_2MnSi	L_{21}	100	4.94	5	6×10^{-5}
Co_2MnGa	L_{21}	67	4.06	4	
Co_2MnGe	L_{21}	100	4.94	5	1.9×10^{-4}
Co_2MnSn	L_{21}	77	4.98	5	7×10^{-4}
Co_2MnSb	L_{21}	100	5.62	6	

used using a static field equal to 2.1 T perpendicular to the films plane (see Refs. 41 and 42 for more details). The measurements were performed near the ferromagnetic resonance frequency, driven by a radio-frequency magnetic field of small amplitude. The FMR results are shown in Fig. 14 for different $\text{Co}_{2-x}\text{Mn}_{1+y}\text{Si}_{1+z}$ films. A drastic change in the dynamic magnetic permeability is observed when going off-stoichiometry: resonance linewidths are strongly affected, as well as the appearance of several peaks that show the occurrence of several magnetic phases within the sample.

This is a clear demonstration that the magnetic properties are extremely sensitive to any stoichiometric deviation in these compounds, where other techniques such as RHEED or XRD are not. Indeed, the final RHEED patterns along [110] azimuth are also shown in Fig. 14 in order to illustrate that this kind of deviation (up to 30% on each element) cannot be detected during the growth. Indeed, no significant differences are observed on RHEED patterns because the surface lattice is still the same (2D square lattice). Moreover, the diffraction streak intensities were very similar for each composition, and the half-streaks (sensitive to the

Mn/Si ordering) were not strongly affected. Hence, in order to explain the physical properties of Heusler compounds, one has to go beyond the simple occurrence of half-streaks on RHEED patterns [or XRD (111) reflection]. One should note that all the FMR resonances observed for off-stoichiometric samples collapse in a unique resonance when reaching the 2:1:1 ratio. So, a first conclusion is that the control of the 2:1:1 ratio is crucial to get only one FMR mode, and thus to extract an accurate estimation of the magnetic damping coefficient. FMR doublets were sometimes observed and interpreted as the consequence of coexistence of two distinct phases (B2 and L_{21} , for example) (reference sample in Ref. 33), but our former analysis shows that it may also originate from stoichiometry deviation (Fig. 14). To disentangle the impact of these two behaviors on FMR, we propose to examine the case where two different chemical phases coexist together with the best control as possible of the 2:1:1 ratio. As Co_2MnSi grows in the L_{21} structure and Co_2MnAl in the B2 one, $\text{Co}_2\text{MnAl}_x\text{Si}_{1-x}$ is a model system to test the FMR response to chemical phases mixing (keeping in mind that the cubic lattice is fixed in the film whatever the x value). A series of 20 nm thick $\text{Co}_2\text{MnAl}_x\text{Si}_{1-x}$ films were thus grown in the same run with $x = 0, 1/4, 1/2, 3/4, \text{ and } 1$. We actually observed such phase mixing by HRTEM.⁴² Typical FMR spectra are shown in Fig. 15 for pure Co_2MnSi , $\text{Co}_2\text{MnAl}_x\text{Si}_{1-x}$ with $x = 1/4$ and pure Co_2MnAl . The first important result to note is the unique FMR transition in single-B2 phase Co_2MnAl ($4\mu_B$ per formula unit) and single- L_{21} phase Co_2MnSi ($5\mu_B$ per f.u.). When the Si and Al phases coexist, two FMR resonance peaks were actually observed depending on the applied magnetic field. This can be explained by the different magnetic moments in each phase. Even if we never observed well-separated transitions, this is a signature of the two phases mixing. Indeed, the origin of this doublet cannot be attributed to any even small deviation to stoichiometry since a unique transition was observed in $\text{Co}_2\text{Mn-Al}$ and $-\text{Si}$. Consequently, we confirm that the coexistence of two phases in $\text{Co}_2\text{MnAl}_x\text{Si}_{1-x}$ may lead to doublets in the FMR response depending on the applied field amplitude.

But is it still the same with a single compound with two phases inside the film? The case of Co_2MnSi polycrystalline film grown on glass substrate allows us to answer this question. We actually observed the coexistence of the B2 and L_{21} within the grains and interestingly only one FMR transition was observed (Fig. 16).⁷⁶ One may argue that structural defects in polycrystalline films on FMR may lead to FMR transition broadening that hides the double transition but this is not true here comparing FMR

**FIG. 14.** VNA-FMR measurements on $\text{Co}_{2-x}\text{Mn}_{1+y}\text{Si}_{1+z}$ films with different x, y, z compositions with $x = y + z$. The corresponding [110] RHEED patterns are inserted.

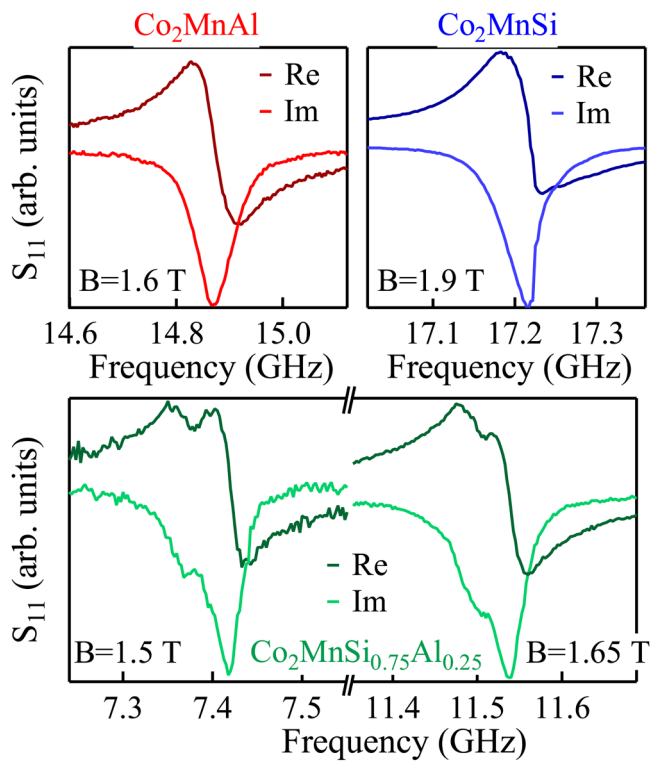


FIG. 15. Comparison of FMR spectra observed in B2- Co_2MnAl , L_{2_1} - Co_2MnSi and mixed B2- L_{2_1} $\text{Co}_2\text{MnAl}_x\text{Si}_{1-x}$ films. A FMR doublet is observed for the bi-phased sample.

spectra in Figs. 15 and 16. This means that the magnetic moments in each phase are the same. This confirms the theoretical work of Pradine *et al.*²⁷ who showed that the magnetic moment in Co_2MnSi is similar for B2 and L_{2_1} chemical ordering. In such a case, the observation of FMR doublets is a signature of off-stoichiometry rather than the coexistence of B2 and L_{2_1} mixed phases. Finally, FMR doublets were observed in irradiated Co_2MnSi films to artificially create 2 phases within the film, i.e., L_{2_1} area surrounded by disordered area.^{33,77} This situation is quite different from what we observed here. Indeed, grain boundaries were created by ion irradiation leading to areas in which A2 phase (random disorder) prevails over the B2 one. In that case, the magnetic moment is certainly strongly affected in the disordered regions and so is the FMR response. To summarize, multiple transitions in FMR may be explained by off-stoichiometric films or/and presence of two phases (or more) with different magnetic moments. This study shows that stoichiometry deviation has to be taken into account as another possible origin of any multiple FMR transitions. However, in the case of two phases with similar magnetic moments within the same lattice (B2 and L_{2_1} in Co_2MnSi), standard FMR is not able to distinguish them. At least, this also highlights the necessity to minimize structural defects in order to get small FMR linewidth and consequently a good estimation of the magnetic damping.

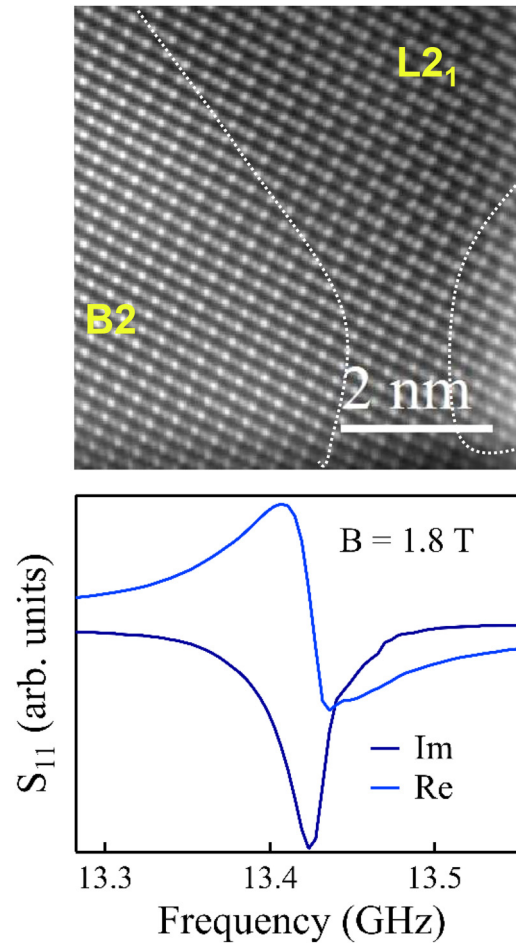


FIG. 16. Example of FMR response on a Co_2MnSi polycrystalline film containing both B2 and L_{2_1} chemical ordering in the grains.⁷⁶ Top, HAADF-STEM image along $[110]$ zone axis and bottom, corresponding FMR spectra.

B. Magnetic moment, spin polarization, and magnetic damping

The magnetic moment in magnetic Heusler films is also very sensitive to structural and chemical ordering, as figured out in many theoretical works.^{17,78,79} A review of the total magnetic moments measured by XMCD and FMR on stoichiometric and off-stoichiometric films is given in Table VI (the element specific spin and orbital moments obtained by XMCD on stoichiometric films are detailed in Appendix C). Theoretical values are also noted. The first important remark is that the total magnetic moment is very sensitive to the stoichiometry. This is not surprising since strong modification of the Mn magnetic moment is predicted depending on its site location in the cubic cell.^{16,27} Thus the average magnetic moment by standard measurement (SQUID, VSM) is an excellent first test of the quality of the films. Naturally, one should also use FMR for that purpose, with the great advantage

TABLE VI. Comparison of Co_2MnZ magnetic moments between calculations, bulk, and thin films. The magnetic moments are given in μ_B per Co_2MnZ unit formula. X indicates no measurement.

	Theory at 0 K ^{6,8}	Bulk ¹²	This study ^{41,68}	
			XMCD	FMR
<i>Single-crystalline Co_2MnZ films</i>				
Co_2MnAl	3.97	4.01	3.83	4.3
Co_2MnSi	4.94	5.07	5.09	5.1
Co_2MnGa	4.06	4.05	5.11	5.4
Co_2MnGe	4.94	5.11	4.48	5.0
Co_2MnSn	4.98	5.08	4.45	5.5
Co_2MnSb	5.62	4.9	x	5.1
<i>Off-stoichiometric $\text{Co}_{2-x}\text{Mn}_{1+y}\text{Si}_{1+z}$</i>				
$\text{Co}_{1.6}\text{Mn}_{1.4}\text{Si}$			x	3.0
$\text{Co}_{1.8}\text{Mn}_{1.6}\text{Si}$			x	4.2
$\text{Co}_{1.9}\text{Mn}_{1.1}\text{Si}$			x	3.9
<i>Poly-crystalline films</i>				
Co_2MnSi		5.07	x	5.0
Co_2MnGa		4.05	x	4.9
Co_2MnGe		5.11	x	4.9

that FMR gives an absolute determination of the magnetic moment of the film alone (contrary to VSM and SQUID measurements that have to be corrected from MgO substrate magnetic contribution⁸⁰ and depend on the uncertainty of the surface of the sample and thickness of the film). Another interesting characteristic is that the Z element is often predicted to be polarized, and antiferromagnetically (AF) coupled with Co and Mn. This was already reported in literature by using XMCD,^{47,81–84} and here we confirmed this induced magnetism and AF coupling at least for Ga and Ge (Appendix C). The last point to address for stoichiometric

samples is that the Slater–Pauling behavior is actually observed in Co_2MnAl , -Si, -Ge, -Sn but not in our Co_2MnGa films (we measured the same value over at least six different samples). This comparison is not relevant for Co_2MnSb since its structure and chemical ordering were not identified in our films. Interestingly, it was not identified in the bulk too.¹² As the magnetic moment, FMR is also very sensitive to the whole magnetic properties of our films. The results are reviewed in Table VII, together with SP measurements already reported in Refs. 3,41,42,68, and 85. This experimental review is now compared with theoretical predictions given in Table V and provides important information in order to reach ultra-low α . First, the spin gap is actually confirmed for type IV Z element (Si, Ge, and Sn but with a small gap), whereas no spin gap was observed for Z = Al. The magnetic damping values are qualitatively correlated with this spin gap occurrence and value (Table VII), the largest the spin gap, the lowest the damping) as suggested based on experimental results^{37,41} and *ab initio* calculations.^{27,75} We recently observed a quantitative link by looking at correlation between SP and α in $\text{Co}_2\text{MnAl}_x\text{Si}_{1-x}$ quaternary alloys.⁶⁸ Indeed, Co_2MnSi grows in the L2₁ structure with a full SP and Co_2MnAl in B2 with SP $\sim 60\%$ (Table VII). Inserting Al in Co_2MnSi is thus a good way to get a mixture of these two phases and consequently to vary the spin polarization. We actually observed such phases mixing by HRTEM allowing us to tune the SP from 100% to 60% as shown by SR-PES. The α values of the series measured by FMR were found to vary linearly with the Al content and hence with the SP, as shown in Fig. 17. To conclude, this is a clear experimental demonstration that the ultra-low magnetic damping obtained in some Heusler compounds is an indirect proof of their HMM behavior. The case of Co_2MnGa is puzzling, since we observed full SP on single-crystalline films with a (001) oriented surface (Table VII) although a lower value was predicted in bulk (Table V). However, its α value was the largest observed among the series (Table VII). Recently, we observed a

TABLE VII. Review of the spin polarization measured by photoemission and magnetic parameters extracted from FMR^{3,41,42,68} (HWHM: half-width at half maximum).

HRTEM structure	Spin polarization (%)	Spin gap (eV)	FMR			
			$\mu_0 M_{\text{eff}} (T)/(\mu_B)$	g	$\alpha (\times 10^{-3})$	HWHM Δf_0 (MHz)
<i>Single-crystalline Co_2MnZ films</i>						
Co_2MnAl B2	63	no	1.07/4.3	2.02	1.10	12
Co_2MnSi L2 ₁	100	0.7	1.31/5.1	2.01	0.46	14
Co_2MnGa L2 ₁	100	~ 0	1.33/5.4	1.96	2.10	102
Co_2MnGe L2 ₁	100	0.5	1.22/5.0	1.99	0.53	24
Co_2MnSn X + L2 ₁	81	0.25	1.20/5.5	2.00	0.91	16
Co_2MnSb ?	36	?	1.14/5.1	2.02	0.96	133
<i>Polycrystalline Co_2MnZ films</i>						
Co_2MnSi B2 + L2 ₁	100	0.7	1.32/5.1	1.99	1.6	7
Co_2MnGe x	90	0.5	1.22/5.0	2.00	1.5	13
Co_2MnGa x	55	no	1.23/4.9	1.95	4.6	121
<i>Off-stoichiometric $\text{Co}_{2-x}\text{Mn}_{1+y}\text{Si}_{1+z}$</i>						
$\text{Co}_{1.6}\text{Mn}_{1.4}\text{Si}$ x	x	X	0.73/2.9	2.00	3.5	220
$\text{Co}_{1.8}\text{Mn}_{1.2}\text{Si}$ x	x	X	1.07/4.2	1.98	1.3	70
$\text{Co}_{1.9}\text{Mn}_{1.1}\text{Si}$ x	x	X	0.96/3.7	1.99	0.7	37

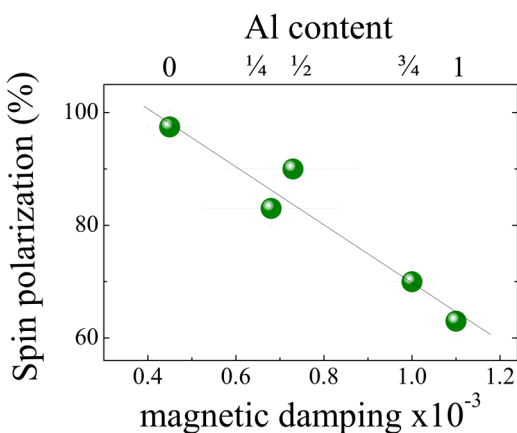


FIG. 17. Correlation between the spin polarization and the magnetic damping in $\text{Co}_2\text{MnAl}_x\text{Si}_{1-x}$ epitaxial films.⁶⁸

much lower SP (55%) on this compound grown as polycrystalline film on glass (Table VII). This point was clarified since according to Co_2MnGa calculated band structure,⁸⁶ the whole Brillouin zone was not probed with our SR-PES measurement conditions in Co_2MnGa single-crystalline films (although the whole BZ is probed for a polycrystalline film).⁶⁸ We thus confirm that Co_2MnGa is not HMM. Nevertheless, this is not sufficient to explain its highest magnetic damping observed in the series, since Co_2MnAl is also not fully polarized although its magnetic damping is lower. There is however one important difference between these two compounds, i.e., the magnetic properties homogeneity Δf_0 is much larger in Co_2MnGa than in Co_2MnAl . This may originate from some antisite disordering^{87,88} difficult to detect by STEM-HAADF due to the small contrast between the elements in Co_2MnGa . There are probably other routes to understand the peculiar properties of our Co_2MnGa thin films compared to the other compounds, since its magnetic moment does not follow the Slater-Pauling behavior (Tables V and VI), and its magnetic anisotropy is the highest among the series. Another puzzling compound is Co_2MnSb , since the SP determined by SR-PES (Table VII) is low compared to the calculated one (Table V), although its magnetic damping is observed to be very low. We explained this SP low value by noting that surface reconstructions due to Sb segregation at the surface were systematically observed by RHEED^{41,68} on the contrary to the other compounds of the series. Indeed, SR-PES is sensitive to the near surface and there is no reason that the spin polarization is conserved when the surface lattice and chemical composition is different from the bulk. As an ultra-low magnetic damping is observed for this compound, we thus emphasized that Co_2MnSb is close to be HMM within the film, i.e., in bulk, as predicted by theory.

VI. CONCLUSIONS AND PERSPECTIVES

In this Tutorial, we looked in detail at the structural and electronic properties of Co_2MnZ Heusler compounds grown as

thin films by molecular beam epitaxy. An accurate control of the stoichiometry was possible thanks to the extremely high sensitivity of quartz microbalance controller available now. In addition, we validate our process control assuming a unity sticking coefficient on the quartz microbalance and on the surface during growth for all the compounds studied here. A bilayer growth mode is systematically observed, even at low temperatures. This means that the basic growing block is a Co cube centered by Mn or Z elements demonstrating the high stability of these Heusler phases. However, a variety of chemical ordering within the FCC lattice is possible, and we show that the observation of (111) peak by x-ray diffraction is not sufficient to claim the occurrence of the L_{21} ordering. STEM-HAADF is shown to be a powerful tool for that purpose. Our results highlight on one hand the key role of the stoichiometry on the electronic properties of these compounds. At least, one can get lower magnetic damping in stoichiometric polycrystalline films than in single-crystalline films prepared with a poor control of the 2:1:1 ratio. On the other hand, the clear correlation between the spin polarization and the magnetic damping observed in $\text{Co}_2\text{MnAl}_x\text{Si}_{1-x}$ alloys is a direct proof of the spin gap as the origin of ultra-low magnetic damping. The lowest magnetic damping coefficients are thus observed when the spin gap is present ($\text{Co}_2\text{Mn-Si}$, $-\text{Ge}$, $-\text{Sn}$ and probably $-\text{Sb}$), and the highest in $\text{Co}_2\text{Mn-Al}$ and $-\text{Ga}$ with no spin gap at the Fermi energy. Another important conclusion of this work in the perspective of applications is that a HMM material keeps its peculiar electronic properties even in polycrystalline films providing a good control of the stoichiometry. The most important issue for applications using the sputtering deposition technique is thus to find some way to control the stoichiometry as best as possible although single-crystal films are not mandatory. If this is certainly the key parameter for applications, this is not the only one issue for applications. Another important goal not addressed here is to get Heusler thin films with perpendicular magnetic anisotropy (PMA).⁸⁹⁻⁹¹ The PMA was obtained in superlattices^{32,34,68} but at least the impact of spin-orbit coupling on the electronic band structure and magnetic damping is still an open question. Getting HMM films with PMA and ultra-low damping will still require significant research efforts in the coming years. Finally, there is a very large variety of Heusler compounds which can have other interesting properties for spintronics. By playing on the chemical elements in the Heusler structure, one can obtain magnetic films with weak magnetic moments (Ni-based Heusler,^{60,92} and even zero for antiferromagnetic or compensated ferrimagnetic compounds.^{93,94} Some half-Heusler compounds were also identified in theory as topological insulators.⁹⁵ The integration of such Heusler compounds in semiconductor-based device is also a challenge.⁹⁶ Finally, these materials also offer the possibility to couple thermoelectric, magnetic and electrical transport properties.⁹⁷ It remains to succeed in preparing these materials in thin films with the required properties. There are still many Heusler compounds possibilities to explore, including quaternary alloys.^{98,99} The number of promising Heusler compounds is so vast that the strong and continuous efforts in *ab initio* calculations (at the origin of this research field) must continue to help the experimentalists in their choice of materials to study.

ACKNOWLEDGMENTS

This work was supported partly by the French PIA project “Lorraine Université d’Excellence,” reference ANR-15-IDEX-04-LUE, by the Agence Nationale de la Recherche (France) under Contract No. ANR-17-CE24-0008 (CHIPMuNCS) and by the “SONOMA” project co-funded by FEDER-FSE Lorraine et Massif des Vosges 2014-2020, a European Union Program.

APPENDIX A: X-RAY DIFFRACTION DETAILS

1. Structure factor calculation

Starting from the four different sites $u = \alpha, \beta, \gamma,$ and δ in the Heusler unit cell (Fig. 18), one is able to calculate the associated structure factor using the equation $F(\mathbf{q}) = \sum_u f_u e^{2i\pi\mathbf{q}\cdot\mathbf{r}_u}$, where F is the structure factor, \mathbf{q} a reciprocal lattice vector, and \mathbf{r}_u represents the position of the u site in the $(\vec{a}, \vec{b}, \vec{c})$ lattice as shown in Table VIII.

It is now easy to obtain the structure factors for the different chemical phases shown in Fig. 1 by using an occupation matrix that defines the occupation rate of the site u by the element,⁵¹ as shown below,

$$f_u = \Gamma f_k \rightarrow \begin{pmatrix} f_\alpha \\ f_\beta \\ f_\gamma \\ f_\delta \end{pmatrix} = \begin{pmatrix} \Gamma_{\alpha\text{Co}} & \Gamma_{\alpha\text{Mn}} & \Gamma_{\alpha\text{Z}} \\ \Gamma_{\beta\text{Co}} & \Gamma_{\beta\text{Mn}} & \Gamma_{\beta\text{Z}} \\ \Gamma_{\gamma\text{Co}} & \Gamma_{\gamma\text{Mn}} & \Gamma_{\gamma\text{Z}} \\ \Gamma_{\delta\text{Co}} & \Gamma_{\delta\text{Mn}} & \Gamma_{\delta\text{Z}} \end{pmatrix} \begin{pmatrix} f_{\text{Co}} \\ f_{\text{Mn}} \\ f_{\text{Z}} \end{pmatrix},$$

where each coefficient Γ_{uk} is the occupation rate of the element on the site u . For instance, the occupation matrix of the B2 phase is

$$\Gamma_{B2} = \begin{pmatrix} 1 & 0 & 0 & 0 \\ 0 & 1 & 0 & 0 \\ 0 & 0 & 1/2 & 1/2 \\ 0 & 0 & 1/2 & 1/2 \end{pmatrix} \rightarrow \begin{cases} f_\alpha = f_\beta = f_{\text{Co}} \\ f_\gamma = f_\delta = \frac{1}{2}f_{\text{Mn}} + \frac{1}{2}f_{\text{Z}} \end{cases}.$$

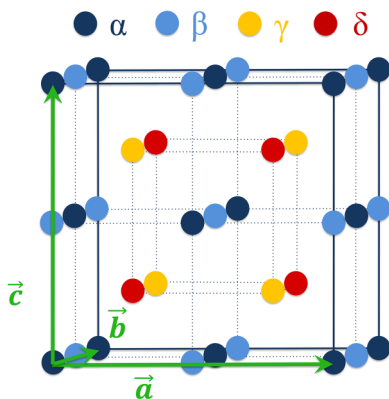


FIG. 18. Heusler $Fm\bar{3}m$ structure and its four different sites.

TABLE VIII. Structure factors $F(hkl)$ expressed according to the four sites shown in Fig. 18.

h,k,l conditions	$F(h,k,l)$
h, k and l evens $h+k+l=4n$	$F = 4[f_\alpha + f_\beta + f_\gamma + f_\delta]$
h, k and l odds $h+k+l=4n+1$	$F = 4[f_\alpha - f_\beta - i(f_\gamma - f_\delta)]$
h, k and l evens $h+k+l=4n+2$	$F = 4[f_\alpha + f_\beta - f_\gamma - f_\delta]$
h, k and l odds $h+k+l=4n+3$	$F = 4[f_\alpha - f_\beta + i(f_\gamma - f_\delta)]$

2. Quantitative analysis

In order to differentiate the chemical ordering using standard x-ray diffraction, a quantitative analysis of the Co_2MnZ XRD reflection intensities is necessary. The intensity of a diffracted peak depends on many parameters as (see, for instance, Ref. 67)

$$I_{\text{Co}_2\text{MnZ}}(hkl) = \frac{\lambda^3 r_0^2 S \tau}{\omega V_C} L P A_f T |F_{\text{Co}_2\text{MnZ}}(hkl)|^2, \quad (A1)$$

where $I_{\text{Co}_2\text{MnZ}}(hkl)$ is the peak intensity, λ is the radiation wavelength, r_0 is the classical electron radius, S is the shined crystal surface, τ is the film thickness, ω is the scanning velocity, V_C is the unit cell volume, L is the Lorentz correction factor, P is the polarization factor, A_f is the absorption factor, T is the thermal diffuse scattering factor, and $F_{\text{Co}_2\text{MnZ}}(hkl)$ is the structure factor of the crystal. Due to this complex equation, intensity simulations are often tricky. We propose here another method of analysis without trying to calculate the peaks intensity, but rather by comparing the intensity of one peak—(222) for example—from one compound to the other, according to the (222) structure factor of the different phases given in Fig. 1. This is possible here because the lattice spacings of the compounds are very close to each other, so a given (hkl) peak is found at similar angles leading to a very similar configuration ($\omega, \lambda, S,$ etc.). All the correction factors are thus considered to be the same for a given (hkl) reflection from one compound to another. This might appear as a crude approximation but one can see that it is well justified in Ref. 67. Thus, the intensity can be expressed as

$$I_{\text{Co}_2\text{MnZ}}(hkl) = \Lambda(hkl) \cdot \frac{\tau}{a^6} |F_{\text{Co}_2\text{MnZ}}(hkl)|^2, \quad (A2)$$

where $\Lambda(hkl)$ is a constant for one given (hkl) reflection for the whole Co_2MnZ series. This means that the square root of the intensity with thickness and lattice constant correction called $A(hkl)$ in the following is proportional to the structure factor as

$$|F_{\text{Co}_2\text{MnZ}}(hkl)| \propto \pm \sqrt{I_{\text{Co}_2\text{MnZ}}(hkl) \frac{a^6}{\tau}} = A_{\text{Co}_2\text{MnZ}}(hkl). \quad (A3)$$

The lattice constant a of each compound is determined by XRD and the layer thickness τ by the different methods described

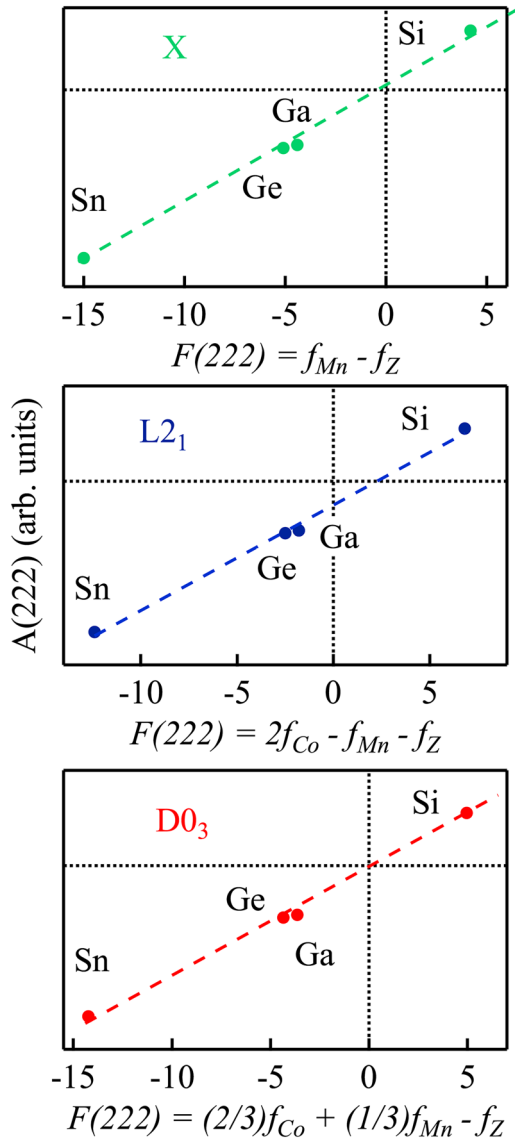


FIG. 19. $A(222)$ parameter obtained for each compound plotted as a function of $F_{Co_2MnZ}(222)$ for the X, L2₁, and D0₃ chemical phases.

above (RHEED, XRR). The next step is to plot the “normalized” intensity A_{Co_2MnZ} as a function of the structure factor F_{Co_2MnZ} for a given (hkl) reflection. Looking in Table VIII, $h + k + l = 4n + 2$ reflections are the most interesting since in that case $F_{Co_2MnZ}^{L2_1} \neq F_{Co_2MnZ}^{D0_3} \neq F_{Co_2MnZ}^X$. Thus, A_{Co_2MnZ} should vary linearly with F_{Co_2MnZ} if all the films are in the same structure. Another way to see the advantage of this method is to look at special situations. Imagine that the structure is L2₁ for Z = Si, Ga, and Ge but not for Sn (that could be in D0₃ or X structures). Thus, a A_{Co_2MnZ} linear variation with $F_{Co_2MnZ}^{L2_1}$ should be observed with Si, Ga, and Ge but the Sn point should not be on this curve since the D0₃

and X structural factors are different. An example of such a quantitative analysis on the (222) reflection is presented in Fig. 19. The scattering amplitudes f_{Co} , f_{Mn} , and every f_Z were taken from the DABAX database,¹⁰⁰ taking into account the incident radiation energy ($K\alpha$ Cu) as well as the anomalous part of the scattering amplitudes with angle corresponding to the reflection.

In Fig. 19, a linear variation is observed for the three chemical phases and does not allow us to identify which one occurs in our series of compounds. Even though this study was not conclusive, it is a demonstration of the difficulty to disentangle these three chemical phases by using only standard diffraction. Moreover, it shows that one cannot claim the L2₁ structure with the simple occurrence of a $4n + 1$ or $4n + 3$ reflections. For more details, see Ref. 68

APPENDIX B: FERROMAGNETIC RESONANCE

In this work, vector network analyzer ferromagnetic resonance (VNA-FMR) is used to study the magnetization precession motion and more precisely the sample’s dynamic magnetic susceptibility tensor (one of its coefficients). The measurement of the dynamic susceptibility allows us to obtain the magnetic damping coefficient value. In the following, we remind some basics regarding FMR measurements, then the experimental geometry used in the present work will be discussed. Finally, we present how the parameters were extracted from the data.

1. FMR Basics

FMR measurements consist in moving the sample magnetization into a precession motion by using an oscillating magnetic field of small amplitude, in the radiofrequency (rf) range. When the frequency of this rf excitation field matches the resonance frequency of the sample, the magnetization starts to oscillate around its equilibrium. The resonance frequency and the precession motion lifetime are not only fixed by the effective field felt by the magnetization, but also by several intrinsic magnetic parameters such as the damping coefficient. These parameters can be obtained through measurements of the dynamic magnetic susceptibility that is the response of the system under the rf excitation. In the linear response regime, the rf excitation field amplitude is much smaller than the static field H_0 applied to saturate the magnetization. When this static field is applied perpendicularly to the film’s plane, and within the low damping approximation, the real and imaginary parts of the χ_{yy} coefficient of the dynamic susceptibility tensor read

$$\chi'_{yy}(\omega) = \gamma_0 M_S \frac{\omega_r(\omega_r^2 - \omega^2)}{(\omega_r^2 - \omega^2)^2 + 4\alpha^2 \omega_r^2 \omega^2}, \quad (B1)$$

$$\chi''_{yy}(\omega) = \gamma_0 M_S \frac{(\alpha \omega_r^2 + \omega^2) \omega}{(\omega_r^2 - \omega^2)^2 + 4\alpha^2 \omega_r^2 \omega^2}, \quad (B2)$$

where α is the magnetic damping coefficient, γ_0 is the gyromagnetic factor, M_S is the saturation magnetization, ω_r is the resonance pulsation with $\frac{\omega_r}{2\pi} = \gamma_0(H_0 - M_{\text{eff}})$ and M_{eff} is the effective magnetization. The real and imaginary parts of the dynamic susceptibility have thus a Lorentzian-like shape, typical of resonance phenomena, where divergence at the resonance frequency is prevented by the

damping term. Moreover, one can see in the expression of χ'_{yy} and χ''_{yy} that the linewidth is equal to $2\alpha\omega_r$. Thus, the study of the resonance frequency and linewidth dependency with the static field allows us to extract the magnetic damping coefficient.

2. Experimental geometry

The VNA generates a rf signal in a broad frequency range (typically 1–40 GHz). The sample lies on a coplanar waveguide (CPW) in which the rf signal creates a rf magnetic field of small amplitude in the y direction. The sample magnetization is saturated with a static magnetic field $B_0 = \mu_0 H_0$, ranging from 0 to 2.5 T and applied perpendicularly to the film's plane. A sketch of the setup is presented in Fig. 20. The dynamic magnetic susceptibility is measured by the VNA for different H_0 steps, via the scattering matrix tensor, which is proved to be directly related to χ .¹⁰¹ The 20 nm thickness of our samples allows us to get an excellent signal-to-noise ratio according to the magnetic moments of our Heusler layers. However, our setup is sensitive enough to measure only several atomic layers of magnetic material.

Two important points on the experimental geometry and setup must be addressed. First, the magnetic damping coefficient measured by FMR is an effective value α_{eff} that contains the intrinsic damping but also extrinsic contributions,

$$\alpha_{eff} = \alpha_{int} + \alpha_{rad} + \alpha_{eddy} + \alpha_{sp} + \dots, \quad (B3)$$

where α_{int} is the intrinsic damping, α_{rad} is the radiative damping term, α_{eddy} is the eddy current damping and α_{sp} is the damping contribution due to spin pumping effect. α_{rad} and α_{eddy} both originate in the coupling of the sample with the CPW, where out of phase currents are generated and re-induced to create out of phase oscillating field. These contributions are complex to estimate¹⁰² and are beyond the goal of our study. α_{sp} on the other hand, comes from the spin currents generated toward the capping layer through spin pumping effect. In our study, the capping layer is Au which has a

small effective spin Hall angle,¹⁰³ thus α_{sp} is assumed to be small. In summary, effective values measured in this study are upper value of the intrinsic magnetic damping coefficient. Second, the perpendicular geometry (static field applied out of plane of the film) was chosen to avoid another extrinsic contribution to the resonance linewidth called the 2-magnon scattering broadening.¹⁰⁴ This geometry is thus pertinent for measuring ultra-low magnetic damping values.

3. Data treatment

An example of FMR measurement on a 20 nm thick Co_2MnSn epitaxial Heusler compound⁶⁸ is shown in Fig. 21. The real and imaginary parts of the dynamic susceptibility were collected [Fig. 21(a)] for different static magnetic field values from 1 to 2.3 T with a 0.05 T step. To determine the resonance frequency and linewidth, both the real and imaginary parts were fitted with a function close to the dynamic susceptibility expression. Then, the resonance frequency as a function of the applied field [Fig. 21(b)] and the full width at half maximum as a function of the resonance frequency [Fig. 21(c)] are plotted. Using the FMR data treatment defined by Kittel¹⁰⁵ in the case of a perpendicular geometry, a linear variation of the transition linewidth Δf with the resonance frequency f_r is obtained. In the literature this transition linewidth is defined using the full-width (Δf_0^{FWHM}) or the half-width (Δf_0^{HWHM}) at half maximum.⁶⁸ These linear variations thus are written as

$$\Delta f^{FWHM} = 2\alpha\gamma_0(H - M_{eff}) + \Delta f_0^{FWHM} = 2\alpha f_r + \Delta f_0^{FWHM} \quad (B4)$$

or

$$\Delta f^{HWHM} = \alpha\gamma_0(H - M_{eff}) + \Delta f_0^{HWHM} = \alpha f_r + \Delta f_0^{HWHM}, \quad (B5)$$

where $\gamma_0 = \frac{g\mu_B}{\hbar}$, H is the applied magnetic field and M_{eff} is the effective magnetization. Using Eq. (B5) (used in this paper, so Δf_0^{HWHM} values are reported), one can have access to the Landé-g factor through γ_0 , here equal to $g = 1.99 \pm 0.01$, the effective

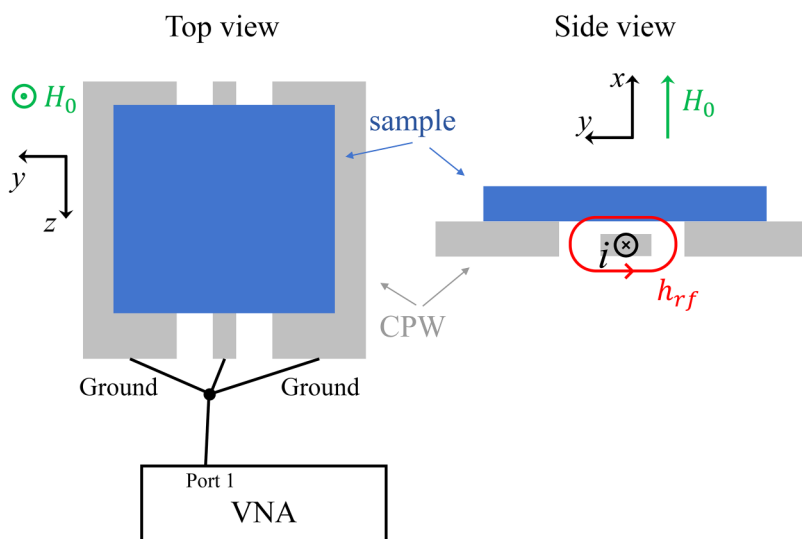


FIG. 20. Sketch of the VNA-FMR setup with the perpendicular geometry.

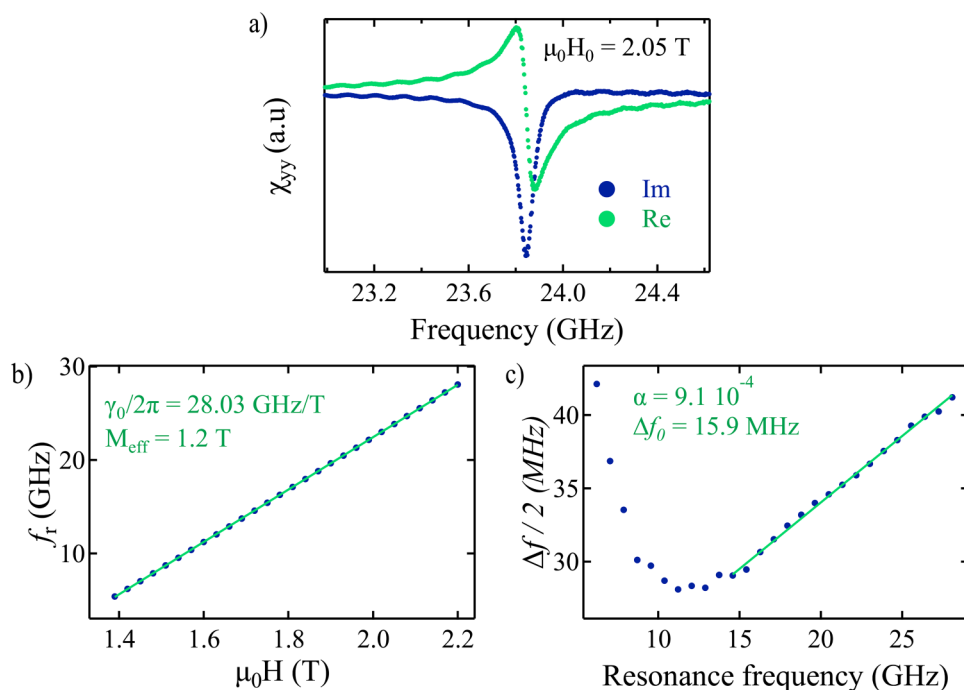


FIG. 21. FMR measurements on a Co_2MnSn epitaxial layer; (a) the real and imaginary parts of the dynamic susceptibility measured with the VNA, (b) plot of the resonance frequency as a function of the applied field for which a linear fit gives us the effective magnetization and Landé-g ratio, (c) plot of the linewidth at half maximum of the resonance peak as a function of the resonance frequency with its linear fit to obtain the magnetic damping.

magnetization $M_{\text{eff}} = 1.2 \text{ T}$, the magnetic damping coefficient $\alpha = 9.1 \times 10^{-4} \pm 1 \times 10^{-4}$, and eventually the inhomogeneous linewidth Δf_0 .⁴¹

APPENDIX C: ELEMENT SPECIFIC MAGNETIC MOMENTS

Total magnetic moments measured by XMCD on our Heusler films are given in Table IX without any details on the element specific moments. The spin and orbital moments per atoms are given in the following table (from Ref. 68). The XMCD experiments were also performed at Ga and Ge 2p edges to evidence the magnetic coupling between Z and Co and Mn, which is predicted to be anti-ferromagnetic (AF).^{5,8,9,27} We actually observed such coupling. The accuracy on the magnetic moment values is around $\pm 10\%$.

TABLE IX. Atomic magnetic moments determined by XMCD in the different CMZ Heusler films.

	XMCD magnetic moments (μ_B)					m_{tot} per formula unit
	Co		Mn		Z coupling	
	m_{spin}	m_{orb}	m_{spin}	m_{orb}		
<i>Stoichiometric Co_2MnZ</i>						
Co_2MnAl	0.92	0.09	1.78	0.03	x	3.83
Co_2MnSi	1.00	0.09	2.87	0.04	x	5.09
Co_2MnGa	0.98	0.09	2.94	0.03	AF	5.11
Co_2MnGe	0.89	0.07	2.55	0.01	AF	4.48
Co_2MnSn	0.88	0.08	2.52	0.01	x	4.45

DATA AVAILABILITY

The data that support the findings of this study are available from the corresponding author upon reasonable request.

REFERENCES

- D. C. Ralph and M. D. Stiles, "Spin transfer torques," *J. Magn. Magn. Mater.* **320**, 1190 (2008).
- R. A. de Groot, F. M. Mueller, P. G. van Engen, and K. H. J. Buschow, "New class of materials: Half-metallic ferromagnets," *Phys. Rev. Lett.* **50**, 2024 (1983).
- S. Andrieu, A. Négache, T. Hauet, T. Devolder, A. Hallal, M. Chshiev, A. M. Bataille, P. Le Fèvre, and F. Bertran, "Direct evidence for minority spin gap in the Co_2MnSi Heusler compound," *Phys. Rev. B* **93**, 094417 (2016).
- S. Ishida, S. Fujii, S. Kashiwagi, and S. Asano, "Search for half-metallic compounds in Co_2MnZ ($Z = \text{IIIb, IVb, Vb}$ element)," *J. Phys. Soc. Jpn.* **64**, 2152 (1995).
- S. Picozzi, A. Continenza, and A. J. Freeman, " Co_2MnX ($X = \text{Si, Ge, Sn}$) Heusler compounds: An *ab-initio* study of their structural, electronic, and magnetic properties at zero and elevated pressure," *Phys. Rev. B* **66**, 094421 (2002).
- I. Galanakis, P. H. Dederichs, and N. Papanikolaou, "Slater-Pauling behavior and origin of the half-metallicity of the full-Heusler alloys," *Phys. Rev. B* **66**, 174429 (2002).
- I. Galanakis, "Appearance of half-metallicity in the quaternary Heusler alloys," *J. Phys. D* **16**, 3089 (2004).
- Y. Kurtulus, R. Dronskowski, G. Samolyuk, and V. Antropov, "Electronic structure and magnetic exchange coupling in ferromagnetic full Heusler alloys," *Phys. Rev. B* **71**, 014425 (2005).
- H. C. Kandpal, G. H. Fecher, and C. Felser, "Calculated electronic and magnetic properties of the half-metallic, transition metal based Heusler compounds," *J. Phys. D* **40**, 1507 (2007).
- Y. V. Kudryavtsev, N. V. Uvarov, V. N. Iermolenko, I. N. Glavatskiy, and J. Dubowik, "Electronic structure, magnetic and optical properties of Fe_2MnGa Heusler alloy," *Acta Mater.* **60**, 4780 (2012).

- ¹¹M. Ram, A. Saxena, A. E. Aly, and A. Shankar, "Half-metallicity in new Heusler alloys Mn_2ScZ ($Z = Si, Ge, Sn$)," *RSC Adv.* **10**, 7661 (2020).
- ¹²P. J. Webster, "Magnetic and chemical order in Heusler alloys containing cobalt and manganese," *J. Phys. Chem. Solids* **32**, 1221 (1971).
- ¹³J. Kübler, G. H. Fecher, and C. Felser, "Understanding the trend in the Curie temperatures of CO_2 -based Heusler compounds: *Ab initio* calculations," *Phys. Rev. B* **76**, 024414 (2007).
- ¹⁴Y. Miura, H. Uchida, Y. Oba, K. Nagao, and M. Shirai, "Coherent tunnelling conductance in magnetic tunnel junctions of half-metallic full Heusler alloys with MgO barriers," *J. Phys. Condens. Matter* **19**, 365228 (2007).
- ¹⁵P. Turban, S. Andrieu, B. Kierren, E. Snoeck, and C. Teodorescu, "A growth and characterisation of single crystalline NiMnSb thin films & NiMnSb/MgO/NiMnSb trilayers," *Traverse Phys. Rev. B* **65**, 134417 (2002).
- ¹⁶S. Picozzi, A. Continenza, and A. J. Freeman, "Role of structural defects on the half-metallic character of Co_2MnGe and Co_2MnSi Heusler alloy," *Phys. Rev. B* **69**, 094423 (2004).
- ¹⁷L. J. Singh, Z. H. Barber, Y. Miyoshi, W. R. Branford, and L. F. Cohen, "Structural and transport studies of stoichiometric and off-stoichiometric thin films of the full Heusler alloy Co_2MnSi ," *J. Appl. Phys.* **95**, 7231 (2004).
- ¹⁸S. Kämmerer, A. Thomas, A. Hütten, and G. Reiss, " Co_2MnSi Heusler alloy as magnetic electrodes in magnetic tunnel junctions," *Appl. Phys. Lett.* **85**, 79 (2004).
- ¹⁹K. Yakushiji, K. Saito, S. Mitani, K. Takahashi, Y. K. Takahashi, and K. Hono, "Current-perpendicular-to-plane magnetoresistance in epitaxial $Co_2MnSi/Cr/Co_2MnSi$ trilayers," *Appl. Phys. Lett.* **88**, 222504 (2006).
- ²⁰T. Ishikawa, T. Marukame, H. Kijima, K.-I. Matsuda, T. Uemura, M. Arita, and M. Yamamoto, "Spin-dependent tunneling characteristics of fully epitaxial magnetic tunneling junctions with a full-Heusler alloy Co_2MnSi thin film and a MgO tunnel barrier," *Appl. Phys. Lett.* **89**, 192505 (2006).
- ²¹T. Ishikawa, H. Liu, T. Taira, K. Matsuda, T. Uemura, and M. Yamamoto, "Influence of film composition in Co_2MnSi electrodes on tunnel magnetoresistance characteristics of $Co_2MnSi/MgO/Co_2MnSi$ magnetic tunnel junctions," *Appl. Phys. Lett.* **95**, 232515 (2009).
- ²²S. Tsunegi, Y. Sakuraba, M. Oogane, N. D. Telling, L. R. Sheldford, E. Arenholz, G. van der Laan, R. J. Hicken, K. Takahashi, and Y. Ando, "Tunnel magnetoresistance in epitaxially grown magnetic tunnel junctions using Heusler alloy electrode and MgO barrier," *J. Phys. D Appl. Phys.* **42**, 195004 (2009).
- ²³H. Liu, Y. Honda, T. Taira, K.-I. Matsuda, M. Arita, T. Uemura, and M. Yamamoto, "Giant tunneling magnetoresistance in epitaxial $Co_2MnSi/MgO/Co_2MnSi$ magnetic tunnel junctions by half-metallicity of Co_2MnSi and coherent tunneling," *Appl. Phys. Lett.* **101**, 132418 (2012).
- ²⁴M. Jourdan, J. Minár, J. Braun, A. Kronenberg, S. Chadov, B. Balke, A. Gloskovskii, M. Kolbe, H. J. Elmers, G. Schönhense, H. Ebert, C. Felser, and M. Kläui, "Direct observation of half-metallicity in the Heusler compound Co_2MnSi ," *Nat. Commun.* **5**, 3974 (2014).
- ²⁵C. Liu, C. K. A. Mewes, M. Chshiev, T. Mewes, and W. H. Butler, "Origin of low Gilbert damping in half metals," *Appl. Phys. Lett.* **95**, 022509 (2009).
- ²⁶A. Sakuma, "First-principles study of the Gilbert damping constants of Heusler alloys based on the torque correlation model," *J. Phys. D* **48**, 164011 (2015).
- ²⁷B. Pradines, R. Arras, I. Abdallah, N. Biziere, and L. Calmels, "First-principles calculation of the effects of partial alloy disorder on the static and dynamic magnetic properties of Co_2MnSi ," *Phys. Rev. B* **95**, 094425 (2017).
- ²⁸M. Oogane, T. Wakitani, S. Yakata, R. Yilgin, Y. Ando, A. Sakuma, and T. Miyazaki, "Magnetic damping in ferromagnetic thin films," *Jpn. J. Appl. Phys.* **45**, 3889 (2006).
- ²⁹M. A. W. Schoen, D. Thonig, M. L. Schneider, T. J. Silva, H. T. Nembach, O. Eriksson, O. Karis, and J. M. Shaw, "Ultra-low magnetic damping of a metallic ferromagnet," *Nat. Phys.* **12**, 839 (2016).
- ³⁰S. Tsunegi, Y. Sakuraba, M. Oogane, K. Takahashi, and Y. Ando, "Large tunnel magnetoresistance in magnetic tunnel junctions using a Co_2MnSi Heusler alloy electrode and a MgO barrier," *Appl. Phys. Lett.* **93**, 112506 (2008).
- ³¹Y. Sakuraba, S. Kokado, Y. Hirayama, T. Furubayashi, H. Sukegawa, S. Li, Y. K. Takahashi, and K. Hono, "Quantitative analysis of anisotropic magnetoresistance in Co_2MnZ and Co_2FeZ epitaxial thin films: A facile way to investigate spin-polarization in half-metallic Heusler compounds," *Appl. Phys. Lett.* **104**, 172407 (2014).
- ³²J. G. Azadani, K. Munira, J. Romero, J. Ma, C. Sivakumar, A. W. Ghosh, and W. H. Butler, "Anisotropy in layered half-metallic Heusler alloy superlattices," *J. Appl. Phys.* **119**, 043904 (2016).
- ³³I. Abdallah, B. Pradines, N. Ratel-Ramond, G. BenAssayag, R. Arras, L. Calmels, J. F. Bobo, E. Snoeck, and N. Biziere, "Evolution of magnetic properties and damping coefficient of Co_2MnSi Heusler alloy with Mn/Si and Co/Mn atomic disorder," *J. Phys. D* **50**, 035003 (2017).
- ³⁴T. L. Brown-Heft, J. A. Logan, A. P. McFadden, C. Guillemard, P. Le Fèvre, F. Bertran, S. Andrieu, and C. J. Palmström, "Epitaxial Heusler superlattice Co_2MnAl/Fe_2MnAl with perpendicular magnetic anisotropy and termination-dependent half-metallicity," *Phys. Rev. Mater.* **2**, 034402 (2018).
- ³⁵J. M. Shaw, E. K. Delczeg-Czirjak, E. R. J. Edwards, Y. Kvashnin, D. Thonig, M. A. W. Schoen, M. Pufall, M. L. Schneider, T. J. Silva, O. Karis, K. P. Rice, O. Eriksson, and H. T. Nembach, "Magnetic damping in sputter-deposited Co_2MnGe Heusler compounds with A_2 , B_2 , and L_2_1 orders: Experiment and theory," *Phys. Rev. B* **97**, 094420 (2018).
- ³⁶T. Kubota, S. Tsunegi, M. Oogane, S. Mizukami, T. Miyazaki, H. Naganuma, and Y. Ando, "Half-metallicity and Gilbert damping constant in $Co_2Fe_xMn_{1-x}Si$ Heusler alloys depending on the film composition," *Appl. Phys. Lett.* **94**, 122504 (2009).
- ³⁷S. Mizukami, D. Watanabe, M. Oogane, Y. Ando, Y. Miura, M. Shirai, and T. Miyazaki, "Low damping constant for Heusler alloy films and its correlation with density of states," *J. Appl. Phys.* **105**, 07D306 (2009).
- ³⁸S. Trudel, O. Gaier, J. Hamrle, and B. Hillebrands, "Magnetic anisotropy, exchange and damping in cobalt-based full-Heusler compounds: An experimental review," *J. Phys. Appl. Phys.* **43**, 193001 (2010).
- ³⁹B. Pigeau, G. De Loubens, O. Klein, A. Riegler, F. Lochner, G. Schmidt, L. W. Molenkamp, V. S. Tiberkevich, and A. N. Slavin, "A frequency-controlled magnetic vortex memory," *Appl. Phys. Lett.* **96**, 132506 (2010).
- ⁴⁰H. T. Nembach, T. J. Silva, J. M. Shaw, M. L. Schneider, M. J. Carey, S. Maat, and J. R. Childress, "Perpendicular ferromagnetic resonance measurements of damping and Landé g -factor in sputtered $(Co_2Mn)_{1-x}Ge_x$ thin films," *Phys. Rev. B* **84**, 054424 (2011).
- ⁴¹C. Guillemard, S. Petit-Watlot, L. Pasquier, C. Rojas-Sanchez, A. Bataille, J. Rault, P. Le Fèvre, F. Bertran, and S. Andrieu, "Ultra-low magnetic damping in Co_2Mn -based Heusler compounds promising materials for spintronic," *Phys. Rev. Appl.* **11**, 064009 (2019).
- ⁴²C. Guillemard, W. Zhang, G. Malinowski, C. de Melo, J. Gorchon, S. Petit-Watlot, J. Ghanbaja, S. Mangin, P. Le Fèvre, F. Bertran, and S. Andrieu, "Engineering $Co_2MnAl_xSi_{1-x}$ Heusler compounds as a model system to correlate spin polarization, intrinsic Gilbert damping and ultrafast demagnetization," *Adv. Mater.* **32**, 1908357 (2020).
- ⁴³W. K. Peria, T. A. Peterson, A. P. McFadden, T. Qu, C. Liu, C. J. Palmström, and P. A. Crowell, "The interplay of large two-magnon ferromagnetic resonance linewidths and low Gilbert damping in Heusler thin films," *arXiv:1909.02738v1 [cond-mat.mtrl-sci]* (2019).
- ⁴⁴G. Li, T. Taira, K. Matsuda, M. Arita, T. Uemura, and M. Yamamoto, "Epitaxial growth of Heusler alloy Co_2MnSi/MgO heterostructures on Ge(001) substrates," *Appl. Phys. Lett.* **98**, 262505 (2011).
- ⁴⁵G. Ortiz, A. García-García, N. Biziere, F. Boust, J. F. Bobo, and E. Snoeck, "Growth, structural, & magnetic characterization of epitaxial Co_2MnSi films deposited on MgO & Cr seed layers," *J. Appl. Phys.* **113**, 043921 (2013).
- ⁴⁶M. Oogane, T. Kubota, H. Naganuma, and Y. Ando, "Magnetic damping constant in Co-based full Heusler alloy epitaxial films," *J. Phys. D* **48**, 164012 (2015).
- ⁴⁷A. Neggache, T. Hauet, F. Bertran, P. Le Fèvre, S. Petit-Watlot, T. Devolder, P. Ohresser, P. Boulet, C. Mewes, S. Maat, J. R. Childress, and S. Andrieu, "Testing epitaxial $Co_{1.5}Fe_{1.5}Ge$ electrodes in MgO-based MTJs," *Appl. Phys. Lett.* **104**, 252412 (2014).

- ⁴⁸A. P. McFadden, T. Brown-Heft, D. Pennachio, N. S. Wilson, J. A. Logan, and C. J. Palmström, "Oxygen migration in epitaxial CoFe/MgO/Co₂MnSi magnetic tunnel junctions," *J. Appl. Phys.* **122**, 113902 (2017).
- ⁴⁹H. Pandey, P. C. Joshi, R. P. Pant, R. Prasad, S. Auluck, and R. C. Budhani, "Evolution of ferromagnetic and spin-wave resonances with crystalline order in thin films of full-Heusler alloy Co₂MnSi," *J. Appl. Phys.* **111**, 023912 (2012).
- ⁵⁰S. Wurmehl and M. Wójcik, "Structural order in Heusler compounds," in *Heusler Alloys* (Springer, 2016), p. 87.
- ⁵¹G. E. Bacon and J. S. Plant, "Chemical ordering in Heusler alloys with the general formula A₂BC or ABC," *J. Phys. F* **1**, 524 (1971).
- ⁵²M. Sicot, S. Andrieu, C. Tiusan, F. Bertran, and F. Montaigne, "On the quality of MBE grown Fe/MgO & Co/MgO(001) interfaces," *J. Appl. Phys.* **99**, 08D301 (2006).
- ⁵³E. Bauer, "Phänomenologische theorie der kristallabscheidung an oberflächen," *Zeitschrift für Kristallographie* **110**, 372 (1958).
- ⁵⁴S. Andrieu, P. Turban, and B. Kierren, "Self-organized homo-epitaxial growth of (001) vanadium assisted by oxygen surface reconstruction," *Surf. Sci.* **651**, 154 (2016).
- ⁵⁵M. P. Delplancke-Ogletree, M. Ye, R. Winand, J. F. De Marneffe, and R. Deltour, "Influences of thermal annealing and humidity exposure on surface structure of (100) single-crystal MgO substrate," *J. Mater. Res.* **14**, 2133 (1999).
- ⁵⁶W. Brawn, in *Applied RHEED—Reflection High-Energy Electron Diffraction During Crystal Growth*, edited by G. Höhler (Springer Tracts in Modern Physics, 1999), Vol. 154.
- ⁵⁷J. J. Harris, B. A. Joyce, and P. J. Dobson, "Oscillations in the surface structure of Sn-doped GaAs during growth by MBE," *Surf. Sci.* **103**, L90 (1981).
- ⁵⁸H. Yang, M. Wassmer, E. Tournié, L. Däweritz, and K. Ploog, "Double period RHEED oscillations during MBE growth of GaAs and AlAs on the GaAs (110) surface," *Surf. Sci.* **331–333**, 479 (1995).
- ⁵⁹M. Itoh, "Relation between surface reconstructions and RHEED intensity oscillations," *Phys. Rev. B* **58**, 6716 (1998).
- ⁶⁰S. V. Faleev, Y. Ferrante, J. Jeong, M. G. Samant, B. Jones, and S. S. Parkin, "Unified explanation of chemical ordering, the Slater-Pauling rule, and half-metallicity in full Heusler compounds," *Phys. Rev. B* **95**, 045140 (2017).
- ⁶¹Y. J. Chen, D. Basiaga, J. R. O'Brien, and D. Heiman, "Anomalous magnetic properties and Hall effect in ferromagnetic Co₂MnAl epilayers," *Appl. Phys. Lett.* **84**, 4301 (2004).
- ⁶²C. D. Damsgaard, M. C. Hickey, S. N. Holmes, R. Feidenhansl, S. O. Mariager, C. S. Jacobsen, and J. B. Hansen, "Interfacial, electrical, and spin-injection properties of epitaxial Co₂MnGa grown on GaAs(100)," *J. Appl. Phys.* **105**, 124502 (2009).
- ⁶³T. Ambrose, J. J. Krebs, and G. A. Prinz, "Epitaxial growth and magnetic properties of single-crystal Co₂MnGe Heusler alloy films on GaAs (001)," *Appl. Phys. Lett.* **76**, 3280 (2000).
- ⁶⁴M. R. Paudel, C. S. Wolfe, H. Patton, I. Dubenko, N. Ali, J. A. Christodoulides, and S. Stadler, "Magnetic and transport properties of Co₂MnSn_xSb_{1-x} Heusler alloys," *J. Appl. Phys.* **105**, 013716 (2009).
- ⁶⁵O. Gaier, J. Hamrle, S. J. Hermsdoerfer, H. Schultheiß, B. Hillebrands, Y. Sakuraba, M. Oogane, and Y. Ando, "Influence of the L₂₁ ordering degree on the magnetic properties of Co₂MnSi Heusler films," *J. Appl. Phys.* **103**, 103910 (2008).
- ⁶⁶H. Lee, Y.-H. Wang, C. K. A. Mewes, W. H. Butler, T. Mewes, S. Maat, B. York, M. J. Carey, and J. R. Childress, "Magnetization relaxation and structure of CoFeGe alloys," *Appl. Phys. Lett.* **95**, 082502 (2009).
- ⁶⁷E. J. Baruchel, J. L. Hodeau, M. S. Lehmann, J. R. Regnard, and C. Schlenker, *Neutron and Synchrotron Radiation for Condensed Matter Studies – Volume 1 : Theory, Instruments and Methods* (Les Editions de Physique, Springer-Verlag, 1993).
- ⁶⁸C. Guillemard, "Half-metal magnets Heusler compounds for spintronics," Ph.D. thesis (University of Lorraine, 2019).
- ⁶⁹M. Oogane and S. Mizukami, "Tunnel magnetoresistance effect and magnetic damping in half-metallic Heusler alloys," *Philos. Trans. R. Soc. A* **369**, 3037 (2011).
- ⁷⁰M. A. Zander, J. Herfort, K. Kumakura, H. P. Schönherr, and A. Trampert, "Epitaxial Heusler alloy Co₂FeSi films on Si(111) substrates grown by molecular beam epitaxy," *J. Phys. D* **43**, 305004 (2010).
- ⁷¹A. L. Kwilu, M. Oogane, H. Naganuma, M. Sahashi, and Y. Ando, "Intrinsic Gilbert damping constant in epitaxial Co₂Fe_{0.4}Mn_{0.6}Si Heusler alloys films," *J. Appl. Phys.* **117**, 17D140 (2015).
- ⁷²C. van der Rest, A. Schmitz, and P. J. Jacques, "On the characterisation of anti-site defects and ordering in off-stoichiometric Fe₂VAl-based Heusler compounds by X-ray anomalous diffraction," *Acta Mater.* **142**, 193 (2018).
- ⁷³B. Ravel, J. O. Cross, M. P. Raphael, V. G. Harris, R. Ramesh, and L. V. Saraf, "Atomic disorder in Heusler Co₂MnGe measured by anomalous x-ray diffraction," *Appl. Phys. Lett.* **81**, 2812 (2002).
- ⁷⁴B. A. Collins, Y. Zhong, Y. S. Chu, L. He, and F. Tsui, "Anomalous x-ray diffraction study of disorders in epitaxial films of the Heusler alloy Co₂MnGe," *J. Vac. Sci. Technol. B* **25**, 999 (2007).
- ⁷⁵J. Chico, S. Keshavarz, Y. Kvashnin, M. Pereiro, I. Di Marco, C. Etz, O. Eriksson, A. Bergman, and L. Bergqvist, "First-principles studies of the Gilbert damping & exchange interactions for half-metallic Heuslers alloys," *Phys. Rev. B* **93**, 214439 (2016).
- ⁷⁶C. Guillemard, S. Petit-Watelot, J.-C. Rojas-Sánchez, J. Hohlfeld, J. Ghanbaja, A. Bataille, P. Le Fèvre, F. Bertran, and S. Andrieu, "Polycrystalline Co₂Mn-based Heusler thin films with high spin polarization and low magnetic damping," *Appl. Phys. Lett.* **115**, 172401 (2019).
- ⁷⁷O. Gaier, J. Hamrle, B. Hillebrands, M. Kallmayer, P. Pörsch, G. Schönhense, H. J. Elmers, J. Fassbender, A. Gloskovskii, C. A. Jenkins, C. Felser, E. Ikenaga, Y. Sakuraba, S. Tsunegi, M. Oogane, and Y. Ando, "Improvement of structural, electronic, and magnetic properties of Co₂MnSi thin films by He⁺ irradiation," *Appl. Phys. Lett.* **94**, 152508 (2009).
- ⁷⁸M. P. Raphael, B. Ravel, Q. Huang, M. A. Willard, S. F. Cheng, B. N. Das, R. M. Stroud, K. M. Bussmann, J. H. Claassen, and V. G. Harris, "Presence of antisite disorder and its characterization in the predicted half-metal Co₂MnSi," *Phys. Rev. B* **66**, 104429 (2002).
- ⁷⁹S. Ahmed, C. Boyer, and M. Niewczas, "Magnetic and structural properties of Co₂MnSi based Heusler compound," *J. Alloys Compd.* **781**, 216 (2019).
- ⁸⁰S. Andrieu, J.-F. Bobo, J. Hubsch, and M. Piecuch, "Magnetic properties of body-centered tetragonal iron/iridium superlattices," *J. Magn. Magn. Mater.* **126**, 349 (1993).
- ⁸¹K. Miyamoto, A. Kimura, K. Iori, K. Sakamoto, T. Xie, T. Moko, S. Qiao, M. Taniguchi, and K. Tsuchiya, "Element-resolved magnetic moments of Heusler-type ferromagnetic ternary alloy Co₂MnGe," *J. Phys. Condens. Matter* **16**, S5797 (2004).
- ⁸²R. Y. Umetsu, T. Nakamura, K. Kobayashi, R. Kainuma, A. Sakuma, K. Fukamichi, and K. Ishida, "Soft x-ray magnetic circular dichroism of L₂₁-type Co₂FeGa Heusler alloy," *J. Phys. D Appl. Phys.* **43**, 105001 (2010).
- ⁸³M. Emmel, A. Alfonsov, D. Legut, A. Kehlberger, E. Vilanova, I. P. Krug, D. M. Gottlob, M. Belesi, B. Büchner, M. Kläui, M. Oppeneer, S. Wurmehl, H. J. Elmers, and G. Jakob, "Electronic properties of Co₂FeSi investigated by X-ray magnetic linear dichroism," *J. Magn. Magn. Mater.* **368**, 364 (2014).
- ⁸⁴C. Felser and A. Hirohata, "Element-Specific magnetic and electronic properties of epitaxial Heusler films," in *Heusler Alloys Properties*, edited by H.-J. Elmers, Growth, Applications Editors (Springer, 2016).
- ⁸⁵See <http://www.synchrotron-soleil.fr/Recherche/LignesLumiere/CASSIOPEE> for the CASSIOPEE beamline.
- ⁸⁶S. Chernov, C. Lidig, O. Fedchenko, M. Jourdan, G. Schönhense, and H. J. Elmers "Band structure tuning of Heusler compounds revisited: Spin- and momentum-resolved electronic structure analysis of compounds with different band filling," *arXiv:1910.05205* (2020).
- ⁸⁷K. Kobayashi, K. Ishikawa, R. Y. Umetsu, R. Kainuma, K. Aoki, and K. Ishida, "Phase stability of B₂ and L₂₁ ordered phases in Co₂YGa (Y = Ti, V, Cr, Mn, Fe) alloys," *J. Magn. Magn. Mater.* **310**, 1794 (2007).
- ⁸⁸G. H. Fecher, H. C. Kandpal, S. Wurmehl, C. Felser, and G. Schönhense, "Slater-Pauling rule and Curie temperature of CO₂-based Heusler compounds," *J. Appl. Phys.* **99**, 08J106 (2006).

- ⁸⁹Z. C. Wen, H. Sukegawa, S. Mitani, and K. Inomata, "Perpendicular magnetization of Co₂FeAl full-Heusler alloy films induced by MgO interface," *Appl. Phys. Lett.* **98**, 242507 (2011).
- ⁹⁰A. Hirohata, W. Frost, M. Samiepour, and J.-Y. Kim, "Perpendicular magnetic anisotropy in Heusler alloy films and their magnetoresistive junctions," *Materials* **11**, 105 (2018).
- ⁹¹M. S. Gabor, M. Nasui, and A. Timar-Gabor, "Perpendicular magnetic anisotropy in Pt/Co-based full Heusler alloy/MgO thin-film structures," *Phys. Rev. B* **100**, 144438 (2019).
- ⁹²T. Graf, C. Felser, and S. S. Parkin, "Simple rules for the understanding of Heusler compounds," *Prog. Solid State Chem.* **39**, 1 (2011).
- ⁹³I. Galanakis and P. Mavropoulos, "Spin-polarization and electronic properties of half-metallic Heusler alloys calculated from first principles," *J. Phys. Condens. Matter* **19**, 315213 (2007).
- ⁹⁴C. Felser, L. Wollmann, S. Chadov, G. H. Fecher, and S. S. Parkin, "Basics and prospective of magnetic Heusler compounds," *APL Mat.* **3**, 041518 (2015).
- ⁹⁵B. Yan and A. de Visser, "Half-Heusler topological insulators," *MRS Bull.* **39**, 859 (2014).
- ⁹⁶J. K. Kawasaki, "Heusler interfaces—Opportunities beyond spintronics?," *APL Mater.* **7**, 080907 (2019).
- ⁹⁷J. Hu, S. Granville, and H. Yu, "Spin-dependent thermoelectric transport in cobalt-based Heusler alloys," *Ann. Phys.* **532**, 1900456 (2020).
- ⁹⁸L. Bainsla and K. G. Suresh, "Equiatomic quaternary Heusler alloys: A material perspective for spintronic applications," *Appl. Phys. Rev.* **3**, 031101 (2016).
- ⁹⁹N. A. Zarkovich, P. Singh, A. V. Smirnov, and D. D. Johnson, "Half-metallic compositional ranges for selected Heusler alloys, submitted in april 2020.
- ¹⁰⁰See <http://ftp.esrf.eu/pub/scisoft/xop2.3/doc/WebHelp/applications/optics/dabax.htm> for "DABAX."
- ¹⁰¹C. Bilzer, "Microwave susceptibility of thin ferromagnetic films: Metrology and insight into magnetization dynamics," Ph.D. thesis (Université Paris Sud, 2007).
- ¹⁰²M. A. W. Schoen *et al.*, "Radiative damping in waveguide-based ferromagnetic resonance measured via analysis of perpendicular standing spin waves in sputtered permalloy films," *Phys. Rev. B* **92**, 184417 (2015).
- ¹⁰³P. Laczowski *et al.*, "Experimental evidences of a large extrinsic spin Hall effect in AuW alloy," *Appl. Phys. Lett.* **104**, 142403 (2014).
- ¹⁰⁴R. D. McMichael *et al.*, "Ferromagnetic resonance linewidth in thin films coupled to NiO," *J. Appl. Phys.* **83**, 7037 (1998).
- ¹⁰⁵C. Kittel, "On the theory of ferromagnetic resonance absorption," *Phys. Rev.* **73**, 155 (1948).